

REVIEW ARTICLE OPEN



Multiscale computational understanding and growth of 2D materials: a review

Kasra Momeni^{1,2,3}, Yanzhou Ji^{4,5}, Yuanxi Wang^{6,7}, Shiddartha Paul¹, Sara Neshani⁸, Dundar E. Yilmaz⁹, Yun Kyung Shin⁹, Difan Zhang⁵, Jin-Wu Jiang¹⁰, Harold S. Park¹¹, Susan Sinnott¹², Adri van Duin⁹, Vincent Crespi^{6,7} and Long-Qing Chen^{3,4,12,13}

The successful discovery and isolation of graphene in 2004, and the subsequent synthesis of layered semiconductors and heterostructures beyond graphene have led to the exploding field of two-dimensional (2D) materials that explore their growth, new atomic-scale physics, and potential device applications. This review aims to provide an overview of theoretical, computational, and machine learning methods and tools at multiple length and time scales, and discuss how they can be utilized to assist/guide the design and synthesis of 2D materials beyond graphene. We focus on three methods at different length and time scales as follows: (i) nanoscale atomistic simulations including density functional theory (DFT) calculations and molecular dynamics simulations employing empirical and reactive interatomic potentials; (ii) mesoscale methods such as phase-field method; and (iii) macroscale continuum approaches by coupling thermal and chemical transport equations. We discuss how machine learning can be combined with computation and experiments to understand the correlations between structures and properties of 2D materials, and to guide the discovery of new 2D materials. We will also provide an outlook for the applications of computational approaches to 2D materials synthesis and growth in general.

npj Computational Materials (2020)6:22; <https://doi.org/10.1038/s41524-020-0280-2>

INTRODUCTION

The perfection and physical properties of atomically thin two-dimensional (2D) materials are extremely sensitive to their synthesis and growth process. Achieving desired characteristics such as structural uniformity, high carrier mobility¹, strong light-matter interactions, tunable bandgap, and flexibility is the main challenge for the synthesis and growth of next generation, electronics-grade 2D materials. A reliable and optimized growth and manufacturing process is essential for the synthesis of 2D materials with uniform properties at the wafer scale, e.g., for application in flexible and transparent optoelectronics.

Two main approaches have been employed for the synthesis of 2D materials, i.e., (i) top-down approaches such as mechanical² and liquid-phase exfoliation that allows scalability³, and (ii) bottom-up approaches such as chemical vapor deposition (CVD) and atomic layer deposition techniques⁴. The former approaches are suitable for mass production of 2D materials but with typically lower quality, whereas the latter approaches can produce high-quality 2D materials but in small amounts. For both types of approaches, the morphology and characteristics of the synthesized 2D materials are very sensitive to the thermodynamic or kinetic conditions⁵ of the growth processes, e.g., heat transfer and mass transfer of source chemical species, chemical reaction kinetics, adsorption of reaction product species on a substrate surface, and nucleation and growth of the resulting 2D materials. The goal of this review is to provide an overview of the main theoretical and computational methods for understanding the

thermodynamics and kinetics of mass transport, reaction, and growth mechanisms during synthesis of 2D materials. We will discuss the possibility of synthesis-by-design of new 2D materials guided by computation to reduce the number of expensive and time-consuming trial-and-error experimentations.

The critical challenge for developing theoretical and computational design tools for the synthesis of 2D materials is the broad range of length and temporal scales involved in their growth process. For example, it may require quantum mechanical and atomistic reactive force-field calculations to determine the activation energies for atomic migration on a surface⁶ and understand the atomistic surface reaction mechanisms⁷, and then a finite element method (FEM) to model the mesoscale mass transport phenomena⁸. Other challenges include incorporating the effects of substrates including the types of substrate defects⁹, the possible wrinkling of 2D films¹⁰, the effect of van der Waals (vdW) interactions at the mesoscale¹¹, and the growth kinetics unique to atomically thin materials¹². Also reproducing quadratic dispersion for the flexural acoustic modes of 2D materials using classical or reactive potentials may not be straightforward, it has been already formulated¹³. Furthermore, a practically useful multiscale model should be computationally efficient, numerically accurate, and, more importantly, able to capture the multi-physical governing relationships among the growth conditions, growth morphology, and materials properties. The eventual goal of developing multiscale computational models is to guide the design of new growth chambers to produce uniform large-area 2D materials.

¹Mechanical Engineering Department, Louisiana Tech University, Ruston, LA 71272, USA. ²Department of Mechanical Engineering, University of Alabama, Tuscaloosa, AL, USA. ³Institute for Micromanufacturing, Louisiana Tech University, Ruston, LA, USA. ⁴Materials Research Institute, The Pennsylvania State University, University Park, PA 16802, USA. ⁵Department of Materials Science and Engineering, The Pennsylvania State University, University Park, PA 16802, USA. ⁶2-Dimensional Crystal Consortium, The Pennsylvania State University, University Park, PA 16802, USA. ⁷Department of Physics, The Pennsylvania State University, University Park, PA 16802, USA. ⁸Department of Electrical Engineering, Iowa State University, Ames, IA 50010, USA. ⁹Mechanical Engineering Department, The Pennsylvania State University, University Park, PA 16802, USA. ¹⁰Shanghai Institute of Applied Mathematics and Mechanics, Shanghai Key Laboratory of Mechanics in Energy Engineering, Shanghai University, Shanghai 200072, China. ¹¹Department of Mechanical Engineering, Boston University, Boston, MA 02215, USA. ¹²Department of Engineering Science and Mechanics, The Pennsylvania State University, University Park, PA 16802, USA. ¹³Department of Mathematics, The Pennsylvania State University, University Park, PA 16802, USA. ✉email: kmomeni@latech.edu

Table 1. Examples of applications of DFT to 2D materials, the DFT-based first-principles methodology, and corresponding experimental observables.

Aspect of growth	First-principles framework	Experimental observable and impact
Thermodynamic stability	Thermochemistry, high-throughput screening	Successful synthesis
Interlayer interaction	Dispersion forces, commensurate supercell construction	Orientation control
Precursor chemistry and kinetics	Transition state theory/NEB, thermochemistry, constrained molecular dynamics	Growth rate, residual gas analysis
Growth front advancement	Kinetic Monte Carlo, edge energetics	Morphology and growth rate, microscopy image of edge structure
Defects	Formation energies	Defect population statistics

ATOMISTIC COMPUTATIONAL METHODS

First-principles calculations

This section discusses the computational approaches based on the density functional theory (DFT). The primary application of DFT in modeling 2D materials is to determine the relative thermodynamic stabilities of different crystal structures of a 2D material by computing their chemical potentials or to identify kinetic pathways by analyzing the energetics of potential transient structures from one stable equilibrium structure to another as thermodynamic conditions change. Examples of applications of DFT to understanding 2D materials and their growth, as well as the corresponding DFT-based first-principles methodologies and the corresponding experimental observables for validation are summarized in Table 1.

Thermodynamic stability. The thermodynamic stability of a 2D material requires its formation energy to be negative. The formation energies of various 2D materials have been efficiently calculated by DFT in combination with high-throughput screening platforms¹⁴. The success of DFT in predicting energies relies on the accuracy of well-tempered approximate exchange-correlation functionals. Standard functionals, e.g., the Perdew-Burke-Ernzerhof parametrization of the generalized gradient approximation exchange-correlation functional (GGA-PBE), accompanied by appropriate corrections¹⁵, describe well the formation and atomization energies. However, they are limited by intrinsic delocalization errors when bonds are stretched, resulting in underestimated reaction barriers¹⁶. A more realistic criterion for a stable 2D material is a low “above-hull” energy¹⁷. Exfoliation energies within 0.2 eV/atom are suggested as a general rule of thumb for the stability in 2D form. A slightly stricter criterion to have low surface energy (<20 meV/Å) is suggested to rule out potential high-surface energy but multi-atom-thick sheets.

Kinetically stabilized 2D Materials. As-grown products may be metastable structures rather than ground-state polytypes¹⁸. The well-known phase-stability competition between the 2H and 1T' types in transition metal dichalcogenides (TMDs) has been studied extensively using DFT. Several possible mechanisms for the 1T'-phase stabilization in the disulfide, including growth-related factors such as the presence of point defects and residual strain, have been elucidated through DFT calculations¹⁹. Phase-stability analysis for the entire group -IV metal dichalcogenide family²⁰ revealed that the 1T' phases are generally more stable for ditellurides. In addition to pure compounds, mixing/segregation behavior and order-disorder transitions in alloys have also been discussed²¹. Within the W/Mo + S/Se/Te combinations, mixing either chalcogens or metals is thermodynamically favorable²², which can be experimentally quantified using the Warren-Cowley order parameters²³. For TMDs, theory predicts that at finite temperatures, the formation of random alloys is favorable. However, kinetically stabilized atomically thin strips of alternating W and Mo in a sulfide alloy have been reported²⁴.

Interlayer/substrate interactions. Accurate description of vdW interactions becomes critical when interlayer sheet-sheet or sheet-substrate interactions are considered, e.g., for identifying the growth orientation. As a non-local effect, vdW forces are not correctly described by DFT with semi-local exchange-correlation functionals and are often corrected by adding pairwise interatomic terms from empirical fittings²⁵, based on charge densities²⁶, or by introducing non-local exchange-correlation functionals, i.e., van der Waals Density Functional²⁷. Thorough testing of these methods has been examined in ref. ²⁸. One common technical problem in this computational approach is that substrates are modeled in a slab geometry where the one surface not in contact with the 2D sheet may host surface states, unless it is passivated. To suppress artificial charge transfer that these may induce, capping using pseudohydrogen²⁹ with fractional charge is often performed. With the advent of new software platforms automating the generation of solid surfaces in combination with stacked 2D sheets and adsorption geometries (e.g., MPInterfaces³⁰), high-throughput screening of possible substrates may lead to a systematic approach to substrate engineering.

Precursor chemistry and kinetics. Transient intermediate states are commonly calculated using transition state theory and the nudged elastic band (NEB) method³¹ by calculating bond dissociation energies or corresponding activation barriers³². One recently attempted approach to capture precursor reaction kinetics is constrained molecular dynamics (MD)³³, where slowly varying coordination constraints are enforced on reacting species to map out free energy barriers, as implemented in VASP³⁴. It is different from NEB calculations in that (1) it calculates free energies at finite temperatures; (2) the final state of the reaction need not to be known; and (3) it has a better numerical stability³⁵. Constrained MD was used to study a sulfur precursor, S₂, reacting with a MoO₃ surface³⁶, concluding that MoO₃ surface vacancies favor the sulfurization process both kinetically and thermodynamically. The downside of constrained MD is that a reaction coordinate is chosen a priori, which may bias the system towards unnatural products with incorrect reaction mechanisms³³ and higher reaction barriers³⁴.

Other methods for sampling of rare events such as nucleation of a new structure include umbrella sampling, transition interface sampling, and metadynamics. The umbrella sampling technique was introduced by Torrie and Valleau³⁷, to improve the sampling of systems with energy landscapes containing high energy barriers. The weighted histogram analysis method³⁸ can be used to analyze a series of umbrella sampling methods. In the transition interface sampling³⁹, the transition region is divided into subregions of intermediate states. The rate constant of a reaction in this method is the multiplication of transition probabilities between different intermediate states. The metadynamics technique was introduced in 2002 and is usually used within an atomistic modeling framework⁴⁰. Selected collective variables of the system not only evolve with time but also periodically leave behind positive Gaussian potentials that are added to the original

Table 2. Typical values of formation energies and migration energy barriers of point defects in 2D materials from atomistic calculations.

Type of 2D materials	Type of point defects	Formation energies	Migration energy barriers
Graphene	Stone-Wales ⁶⁰	~5 eV	
	SV ⁶¹	~7.5 eV	~1.5 eV
	V ₂ (5-8-5) ⁵⁶	~8 eV	~7 eV
	V ₂ (555-777) ⁵⁶	~7 eV	~7 eV
	V ₂ (5555-6-7777) ⁵⁶	7 ~ 8 eV	~7 eV
Phosphorene	SV ¹⁹⁵	~1.65 eV	~0.4 eV
MoS ₂	V _S ^{59,60}	1.22 ~ 2.25 eV	~2.27 eV

potential energy of the system, which effectively push the system out of a local minimum and into a neighboring energy well. Informally, metadynamics resembles “filling the free energy wells with computational sand.”⁴¹

Growth front advancement. Early studies focused on calculating the surplus energies of edges in the high-symmetry directions and then applying the thermodynamic Wulff construction⁴². One difficulty in calculating the edge energies is the polar and non-centrosymmetric nature of materials, where the usual ribbon calculation geometry makes the energies of dislike edges inseparable. The usual workaround is by constructing triangular flakes exposing a single type of edge⁴³. Another “energy density method” was introduced in ref. ⁴⁴ and a recently proposed method⁴² aimed at finding a general method suitable for high-throughput calculations introducing capping groups to passivate a surface.

One major criticism of further employing thermodynamic Wulff constructions is that growth is by definition out of equilibrium. Therefore, edges that dominate over others should not be the energetically favorable ones, but the slowest growing ones. The step-flow approach was formulated in ref. ⁴⁵ for graphene growth and was further developed in ref. ⁴⁶ for polar materials, establishing the use of kinetic Wulff construction. A similar approach involves DFT calculations and fitting to experimental grain morphologies, to construct a kinetic Monte Carlo (KMC) model⁴⁷.

Defects. The formation of defects may occur within thermodynamic equilibrium such as thermally generated point defects or follow from growth imperfections such as dislocations and grain boundaries (GBs), or reflect the finite size of crystals such as edges and surfaces. Defects can also be deliberately introduced using methods such as electron or ion irradiation and chemical treatment⁴⁰. The calculation of defect formation energies follows a well-established procedure detailed in ref. ⁴⁸. 2D materials also host lattice-specific defect types, such as the Stone-Wales defect in graphene⁴⁹. Single-atom vacancies are another type of defects in 2D materials. A general strategy to ensure correct convergence behavior for charged defects in 2D systems is presented in ref. ⁵⁰. Defect formation energies in MoS₂ have been comprehensively studied in ref. ⁵¹; possible strategies of introducing extrinsic dopants have been examined in ref. ⁵². Defect complexes are also frequently studied to identify likely combinations between simple intrinsic defects and external contamination⁵³, devise possible defect-pairing strategies to neutralize harmful defects⁵⁴, and investigate their influence on the growth behavior of 2D materials on a different 2D sheet^{9,55}. Multiple vacancies may exist in 2D materials such as double vacancies in graphene, resulting in (i) two pentagons and one octagon—V₂ (5-8-5) defect; or (ii) three pentagons and three heptagons—V₂(555-777) defect; or (iii) four pentagons, a hexagon, and four heptagons—V₂(5555-6-7777) defect⁵⁶. The formation of defects with an even number of vacancies in graphene is energetically favorable due to the lack of

any dangling bonds⁵⁷, whereas a large number of vacancies may bend and wrap the 2D material⁵⁸. Table 2 lists the typical values of formation and migration energies of these point defects from atomistic calculations.

Dislocations are line defects in 2D materials that can be of in-plane edge or out-of-plane screw type. The former consists of pentagon–heptagon (5–7) pairs^{59,60} and the latter makes the structure to become 3D⁶¹. In general, dislocations in 2D materials have high gliding energy barriers and are immobile at room temperature. They hinder the plastic deformation of 2D materials⁶². The in-plane edge dislocations with the smallest Burgers vector, $\mathbf{b} = (1,0)$, is typically the energetically most favorable dislocation configuration. The trilayer bi-atomic MoS₂ has a complex dislocation structure with two types, i.e., Mo-rich that resembles (5–7) and S-rich that resembles (7–5) pairs. The complex nature of dislocations in MoS₂ is a source of its rich chemistry. For example, at specific chemical potentials of S, the (5–7) dislocation reacts with 2S vacancies to form a (4–6) defect.

GBs in 2D materials can be considered as an array of dislocations, which can be divided into low-angle and high-angle GBs depending on the dislocation core density. Atomistic simulations revealed that the mechanical properties of 2D materials, similar to the one-dimensional nanostructures, will be affected by both the density and arrangement of the defects⁶³. Notably, graphene sheets with high-angle tilt GBs can be as strong as the pristine material and much stronger than those with low-angle GBs⁶⁴. First-principles calculations also revealed that sinuous GB structures are energetically favorable when the straight GB line cannot bisect the tilt angle⁶⁵. GB energies of different 2D materials are also reported based on atomistic calculations. For MoS₂, the energy of GB with a 20.6° misorientation angle is 0.05 eV/Å⁶². The GB energy for phosphorene varies between 0.05 and 1.5 eV/Å, depending on its tilt angle⁶⁶.

Molecular dynamics

The MD approach is one of the main tools that have been used to study the growth of 2D materials at the atomistic scale. The quality of potential function governing the atomic interactions is the key for the accuracy of this technique in predicting the structures and properties of 2D materials. In general, two classes of interatomic potentials are used in MD simulations to study the growth of 2D materials, i.e., empirical and reactive potentials, which we elaborate on here.

Empirical potentials. Empirical potentials are faster and more computationally efficient, but less accurate than reactive potentials. Common empirical potentials for modeling 2D materials are reviewed below.

Lennard-Jones potential: In 1924, Lennard-Jones (LJ) published the 12–6 pairwise potential to describe the vdW interaction between two neutral particles (i.e., rare gases)⁶⁷,

$$V_{LJ} = 4\epsilon \left[\left(\frac{\sigma}{r} \right)^{12} - \left(\frac{\sigma}{r} \right)^6 \right] \quad (1)$$

where r is the distance between two interacting atoms, ϵ is the potential well depth and σ is the distance at which the potential is zero. The r^{-12} term captures the strong repulsion occurring when two atoms get closer. The repulsive effect originates from the Pauli exclusion principle, which penalizes the overlap of electron orbitals. The r^{-6} term describes the vdW interaction, which is due to the coupling between the instantaneous polar charges induced in two neutral molecules and is significantly weaker than the electron overlap effects.

The popularity of the LJ potential is due to its simplicity and it has been widely applied to simulate the interlayer interactions in atomically layered materials. While being used to capture vdW interactions, a limitation of the pairwise interaction is the inability to capture frictional processes, such as the sliding of atomic layers.

Table 3. List of common substrates that have been used to grow 2D materials.

TMDs	Substrate
MoS ₂	Sapphire (Al ₂ O ₃) ⁷⁶ , SiO ₂ ⁷⁶ , Graphene ⁷⁷ , SiC ⁷⁸ , hBN ⁷⁹
MoSe ₂	Sapphire (Al ₂ O ₃) ⁸⁰ , SiO ₂ ⁸¹ , Graphene ⁷⁷
WS ₂	SiO ₂ ⁸¹ , Sapphire (Al ₂ O ₃) ⁸¹ , hBN ¹⁹⁶ , Graphene ¹⁹⁷
WSe ₂	SiO ₂ ¹⁹⁸ , Sapphire (Al ₂ O ₃) ¹⁹⁹ , hBN ²⁰⁰
NbS ₂	SiO ₂ /Si ²⁰¹ , Sapphire (Al ₂ O ₃) ²⁰²
NbSe ₂	h-BN ²⁰³ , Graphene ²⁰⁴
MoTe ₂	SiO ₂ ²⁰⁵

h-BN hexagonal boron nitride.

Table 4. List of σ (Å) values of the LJ interactions for different substrates.

	Si	O	C	Al	B	N
Mo	3.27 ²⁰⁶	2.93 ²⁰⁶	3.054 ²⁰⁷	2.570 ²⁰⁸	3.827 ²⁰⁹	3.725 ²⁰⁹
W	0.094 ²¹⁰	1.75 ²¹¹	3.9 ²⁰⁹	2.865 ²⁰⁹	3.927 ²⁰⁹	3.825 ²⁰⁹
S	3.71 ²⁰⁶	3.37 ²⁰⁶	4.00 ²¹²	2.23 ²⁰⁹	3.292 ²⁰⁹	3.75 ²¹²
Se	2.03 ²¹³	3.37 ²⁰⁹	3.585 ²⁰⁷	2.555 ²⁰⁹	3.617 ²⁰⁹	3.515 ²⁰⁹
Te	2.60 ²¹³	3.772 ²⁰⁹	3.847 ²⁰⁹	2.812 ²⁰⁹	3.874 ²⁰⁹	3.772 ²⁰⁹
Nb	3.5855 ²⁰⁹	3.1525 ²⁰⁹	3.9 ²⁰⁹	2.3375 ²⁰⁹	3.399 ²⁰⁹	3.2975 ²⁰⁹

Different corrections have been proposed to overcome this shortcoming^{68–70}. The two potential parameters ϵ and σ can be determined by using one energy quantity like the binding energy and a structural quantity like the density. The LJ parameters for most elements can be determined systematically, as demonstrated by Rappe et al.⁷¹. The LJ parameters for typical 2D materials and substrates in Table 3 are listed in Table 4 (for σ) and Table 5 (for ϵ), respectively.

Stillinger-Weber potential: Stillinger and Weber (SW) proposed this potential in 1985, to model bulk silicon⁷². The SW potential includes both pair (two-body) and three-body interactions,

$$V_2 = Ae^{\rho/(r-r_{\max})} (B/r^4 - 1), V_3 = Ke^{\rho_1/(r_{12}-r_{\max12})+\rho_2/(r_{13}-r_{\max13})} (\cos\theta - \cos\theta_0)^2, \quad (2)$$

where V_2 describes the pairwise bond-stretching energy and V_3 captures the bending energy associated with an angle with initial value θ_0 .

The cut-offs $r_{\max1}$, $r_{\max12}$, and $r_{\max13}$ can be determined by fitting to the average of the first- and second-neighboring bond lengths. The seven unknown potential parameters, including five unknown geometrical parameters, i.e., ρ and B in V_2 and ρ_1 , ρ_2 , and θ_0 in V_3 , and two energy parameters A and K , can be determined either by a least-squares fit to targeted quantities such as the elastic constants, Poisson's ratio, and the phonon spectrum, or by analytical derivations from the linear valence force-field potential. It is noteworthy that the nonlinear parameter B could not be determined by the latter approach, which should be determined by nonlinear quantities such as the third-order elastic constants⁷³.

The SW potential can describe nonlinear processes including large deformations, as higher-order terms for the variation of bond length and angle are included in its formulation. Although the SW potential is efficient and suitable for simulating thermal transport and other nonlinear phenomena⁷⁴, it is not able to describe chemical bond formation or breaking. It should also be noted that the SW potential cannot provide bending energy for atomically layered materials without out-of-plane bonds such as

graphene⁷⁵. Due to its efficiency, the SW potential has been used in the simulation of many atomically layered materials such as 2D nanostructures of Si and their thermal properties⁷⁶, MoS₂^{73,74,76}, MoSe₂⁷⁶, WS₂⁷⁷, and black phosphorus^{73,78,79}. The SW potential has been parametrized for 156 emerging atomic layered materials, along with other available empirical potentials for these atomically layered materials⁸⁰.

Force-field potential: The force-field (FF) potential describes the variation in the potential energy of a deformed structure with respect to its equilibrium configuration. It is essentially a Taylor expansion of the total energy in terms of the variation in the bond length and angle,

$$V = V_b + V_\theta + V_\phi + V_\gamma + V_c + V_{ij} + V_{el}, \quad (3)$$

$$V_b = \sum_i k_b (\Delta b_i)^2 + \sum_i k_b^{(3)} (\Delta b_i)^3 + \sum_i k_b^{(4)} (\Delta b_i)^4, \quad (4)$$

$$V_\theta = \sum_i k_\theta (\Delta\theta_i)^2 + \sum_i k_\theta^{(3)} (\Delta\theta_i)^3 + \sum_i k_\theta^{(4)} (\Delta\theta_i)^4, \quad (5)$$

$$V_\phi = \sum_i k_\phi (\Delta\phi_i)^2, \quad (6)$$

$$V_\gamma = \sum_i k_\gamma (\Delta\gamma_i)^2, \quad (7)$$

$$V_c = \sum_{ij} k_{bb'} (\Delta b_i) (\Delta b'_j) + \sum_{ij} k_{\theta\theta'} (\Delta\theta_i) (\Delta\theta'_j) + \sum_{ij} k_{b\theta} (\Delta b_i) (\Delta\theta_j), \quad (8)$$

where Δb , $\Delta\theta$, $\Delta\phi$, and $\Delta\gamma$ are variations of the bond length, bond angle, twisting angle, and inversion angle, respectively; k_b , $k_b^{(3)}$, $k_b^{(4)}$, k_θ , $k_\theta^{(3)}$, $k_\theta^{(4)}$, k_ϕ , k_γ , $k_{bb'}$, $k_{\theta\theta'}$, and $k_{b\theta}$ are force constants. V_b is the bond-stretching energy, V_θ is the bond angle-bending energy, V_ϕ is the torsional energy for a bond, V_γ is the inversion energy among four atoms, and V_c is the off-diagonal coupling interaction. It is noteworthy that the cubic and quartic anharmonic terms in the bond-stretching and angle-bending interactions enable the FF model to capture nonlinear phenomena such as thermal expansion and thermal transport.

The FF potential has two significant features: (i) the number of interaction terms and (ii) the force-constant parameters and the equilibrium structural parameters (bond lengths and angles). MM3⁸¹ and COMPASS⁸² use all of the interaction terms and can simulate large deformations and nonlinear phenomena. In contrast, the Keating model⁸³ is the simplest model including only the harmonic terms. Parameters of the potential are usually fitted to available data and, thus, the volume and accuracy of the fitted data set determine the accuracy of the FF model. Several generations of FF models have been developed as more data become available, including four versions of the molecular mechanics FF: MM1⁸⁴, MM2⁸⁵, MM3⁸¹, and MM4⁸⁶. The UFF⁷¹ provides the FF parameters for all the elements in the periodic table.

As the energies in the FF model are additive, this potential has been widely used to calculate physical or mechanical properties for various materials via analytic expressions, including many 2D materials. For example, an FF model, with bond stretching and angle-bending terms, has been used to derive the phonon dispersion of graphene layers⁸⁶. The bond-stretching and angle-bending terms were utilized to extract the bending properties of graphene⁸⁷. A mapping between the FF model and the elastic beam model has been developed, which is used to derive analytic expressions for Young's modulus and Poisson's ratio of graphene and carbon nanotubes⁸⁸.

Table 5. List of ε (eV) values of the LJ interactions for different substrates.

	Si	O	C	Al	B	N
Mo	0.00562 ²⁰⁶	0.004 ²⁰⁶	0.003325 ²⁰⁷	0.00585 ²⁰⁸	0.00155 ²⁰⁹	0.00208 ²⁰⁹
W	0.00835 ²⁰⁹	0.006035 ²⁰⁹	0.003862 ²⁰⁹	0.00478 ²⁰⁹	0.00406 ²⁰⁹	0.00543 ²⁰⁹
S	0.00562 ²⁰⁶	0.00884 ²⁰⁶	0.00750 ²¹²	0.00889 ²⁰⁹	0.00755 ²⁰⁹	0.007762 ²¹²
Se	0.86 ²¹³	0.0114 ^{209,214,215}	0.00758 ²⁰⁷	0.00905 ^{209,214,216}	0.00767 ²⁰⁹	0.01033 ²⁰⁹
Te	1.01 ²¹³	0.0114 ^{209,215,217}	0.03104 ²⁰⁹	0.0327 ²⁰⁹	0.00766 ²⁰⁹	0.0334 ²⁰⁹
Nb	0.05115 ²⁰⁹	0.037 ²⁰⁹	0.023651 ²⁰⁹	0.0293 ²⁰⁹	0.0248 ²⁰⁹	0.03325 ²⁰⁹

Reactive interatomic potentials. The reactive-potential approach has been widely used to explore the synthesis and properties of different materials. The reactive potentials can capture the bond breaking and formation during the classical simulations of 2D materials. They are also computationally less expensive than first-principles methods such as DFT calculations and ab-initio MD. Typical reactive potentials that have been frequently considered are Tersoff Bond Order (Tersoff)⁸⁹, Reactive Empirical Bond Order (REBO)⁹⁰, Adaptive Intermolecular Reactive Empirical Bond Order (AIREBO)⁹¹, Charge Optimized Many-Body (COMB)⁹², and Reactive Force Field (ReaxFF)⁹³. These different reactive potentials are reviewed in detail in ref. ⁹⁴. Performances of several reactive and non-reactive potentials in graphene-based materials are compared in ref. ⁹⁵. These potentials allow the realization of the thermodynamic stability of graphene-based materials under different conditions, environmental chemistry, substrate, interlayer interactions, and structural defects. However, only a few of them have been employed in the study of computational synthesis of other 2D materials to reveal thermodynamic stability, simulate the process of the growth of layers, model the top-down synthesis of 2D materials such as exfoliation techniques³⁸, and evaluate the properties of 2D nanostructures. This is due to several challenges including the following: (1) the long time required to develop a reactive potential, (2) the non-transferability of potential parameters from one material to another, and (3) the lack of universal functional forms for the reactive potentials.

The Tersoff potentials are mainly used to explore various structures and properties of 2D hexagonal boron nitride (h-BN) materials⁹⁶. The REBO and AIREBO potentials are used to simulate the CVD process and growth of 2D amorphous carbon on substrates, mechanical properties of MoS₂, and even study the thermal stability of C₆₀ 2D nanostructures⁹⁷. The COMB3 potentials have been used to simulate the experimental CVD deposition and growth of graphene and metal on substrates⁹⁸. The ReaxFF potentials have been used to explore the structures of several 2D materials under intercalation, study the defects and groups on the surfaces of MXene materials, simulate CVD growth of MoS₂ layers, and explore the synthesis of 2D polymeric materials in experiments^{7,99}. In general, COMB3 and ReaxFF can further explore 2D materials, as their functional forms can describe heterogeneous systems. It remains crucial to find accelerated methods to develop reactive potentials with high accuracy and transferability for 2D materials.

Tersoff potential: The Tersoff potential was first published in 1986¹⁰⁰ and further developed in 1988¹⁰¹. The second version of the Tersoff potential has the following form,

$$E = \sum_i E_i = \frac{1}{2} \sum_{i,j \neq i} V_{ij}, \quad (9)$$

$$V_{ij} = f_C(r_{ij}) [a_{ij} f_R(r_{ij}) + b_{ij} f_A(r_{ij})]; f_R(r) = Ae^{-\lambda_1 r}; f_A(r) = -Be^{-\lambda_2 r}, \quad (10i-iii)$$

where $f_R(r_{ij})$ and $f_A(r_{ij})$ are the repulsive and attractive components, respectively. The cutoff function is:

$$f_C(r) = \begin{cases} 1 & r < R - D \\ \frac{1}{2} - \frac{1}{2} \sin[\frac{1}{2} \pi (r - R) / D] & R - D < r < R + D \\ 0 & r > R + D \end{cases} \quad (11)$$

A distinct feature of the Tersoff potential is the absence of an explicit three-body interaction term. Instead, the concept of bond order is introduced, in which the strength of a given bond depends strongly on its local environment. Bond order is accounted for via the function b_{ij} , which has the following form

$$b_{ij} = (1 + \beta^n \zeta_{ij}^n)^{-1/2n}; \zeta_{ij} = \sum_{k \neq i,j} f_C(r_{ik}) g(\theta_{ijk}) e^{\lambda_3 (r_{ij} - r_{ik})^3}; \quad (12)$$

$$g(\theta) = 1 + \frac{c^2}{d^2} - \frac{c^2}{d^2 + (h - \cos \theta)^2}.$$

a_{ij} is an alternative parameter to improve the accuracy of the potential, with a similar form

$$a_{ij} = (1 + a^n \eta_{ij}^n)^{-1/2n}; \quad (13)$$

$$\eta_{ij} = \sum_{k \neq i,j} f_C(r_{ik}) e^{\lambda_3 (r_{ij} - r_{ik})^3}$$

The 13 unknown parameters are typically determined by fitting to data from first-principles calculations or experiments.

The Tersoff potential was used for modeling of graphene, which gives a better description of the phonon spectrum¹⁰². It was also used to model germanene¹⁰³ and silicene¹⁰³. By introducing one scaling parameter for the quantity b_{ij} with atoms i and j of different elements¹⁰⁴, the Tersoff potential was generalized to describe the interaction for multicomponent systems including C-Si and Si-Ge¹⁰⁴, and boron nitride¹⁰⁵. Using the Tersoff potential, the thermal conductivity of silicene was calculated to be 61.7 and 68.5 W mK⁻¹ for the armchair and zigzag configurations, which is reduced when it is doped with heavier silicon isotopes¹⁰⁶. This potential has also been used for modeling the misfit dislocations in 2D materials, where a critical thickness was found for the formation of an interface misfit dislocation¹⁰⁷.

ReaxFF potential: The ReaxFF⁹³ is a bond-order-based force field, which allows formation and breaking of bonds. It has a general form of

$$E_{\text{system}} = E_{\text{bond}} + E_{\text{over}} + E_{\text{under}} + E_{\text{lp}} + E_{\text{val}} + E_{\text{tor}} + E_{\text{vdW}} + E_{\text{Coulomb}}, \quad (14)$$

where the energy terms on the right-hand side in the order of appearance are bond, over-coordination penalty, under-coordination stability, lone pair, valence, torsion, non-bonded vdW interactions, and Coulomb energies, respectively. The bond-order parameter determines the bonded interactions between the

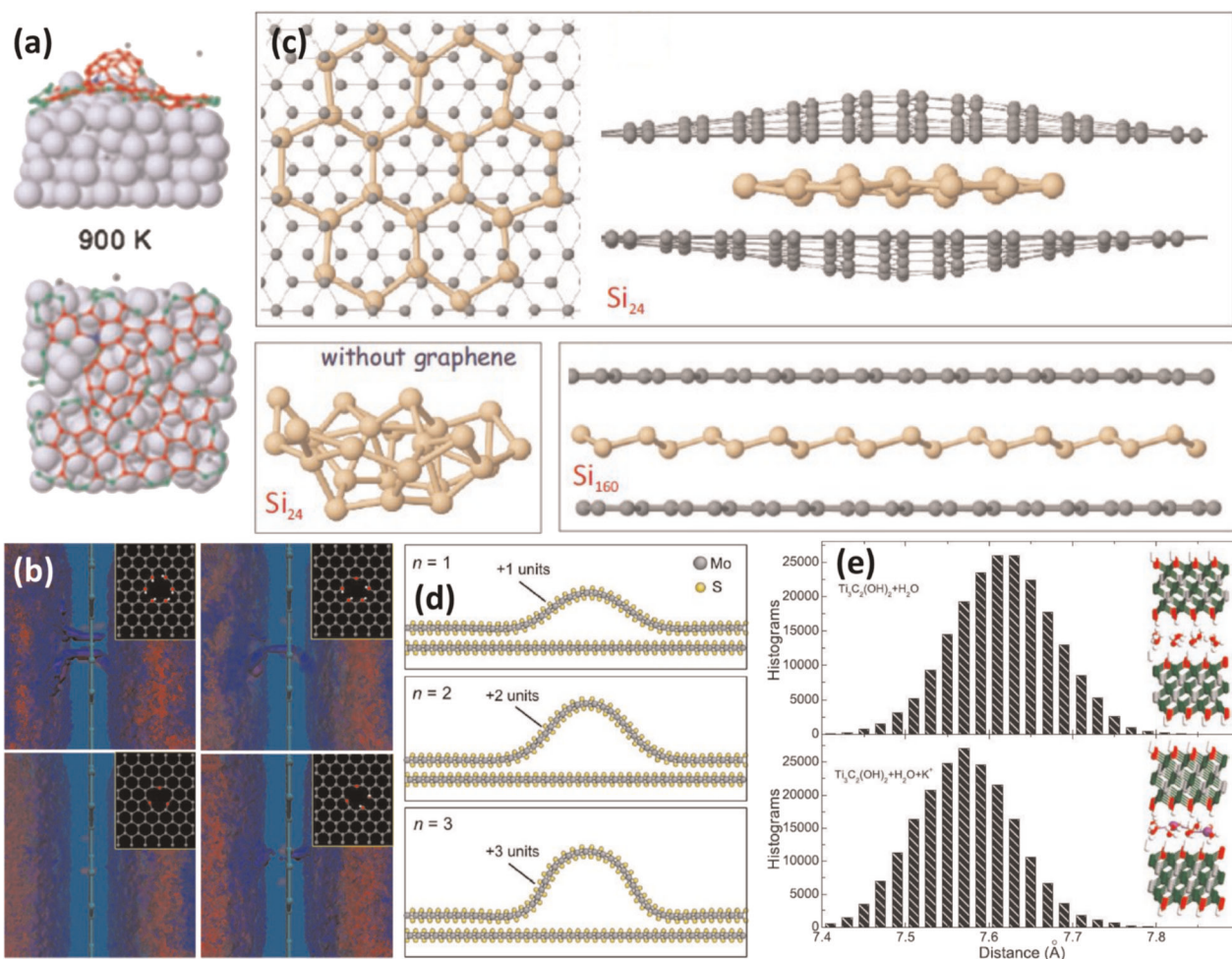


Fig. 1 Application of the ReaxFF method to various 2D materials. **a** Ni-catalyzed growth of single-layer graphene on a Ni(100) surface using MD/UFMC simulations. [Adapted from ref. ¹¹¹ with permission from The Royal Society of Chemistry]. **b** Water-mediated proton transfer through O/OH-terminated vacancy defects on a graphene layer. [Adapted from ref. ¹¹² under Creative Commons Attribution 4.0 International License]. **c** Formation of silicene between graphene bilayers. [Reprinted figure with permission from ref. ¹¹⁴. Copyright (2019) American Chemical Society]. **d** Atomic structures of ripplocations with different numbers of extra units added on top MoS₂ layer. [Adapted with permission from ref. ¹¹⁶. Copyright (2019) American Chemical Society]. **e** Histograms corresponding to averaged interlayer distance without and with K⁺ ions [Reprinted from ref. ¹²¹. Copyright (2019), with permission from Elsevier].

atoms in the system,

$$\begin{aligned} \text{BO}_{ij}^n &= \text{BO}_{ij}^\sigma + \text{BO}_{ij}^\pi + \text{BO}_{ij}^{\pi\pi} \\ &= \exp\left[p_{bo1}\left(\frac{r_{ij}}{r_o^\sigma}\right)^{p_{bo2}}\right] + \exp\left[p_{bo3}\left(\frac{r_{ij}}{r_o^\pi}\right)^{p_{bo4}}\right] + \exp\left[p_{bo5}\left(\frac{r_{ij}}{r_o^{\pi\pi}}\right)^{p_{bo6}}\right], \end{aligned} \quad (15)$$

where BO_{ij}^σ , BO_{ij}^π , and $\text{BO}_{ij}^{\pi\pi}$ are the partial contributions of associated σ , π , and $\pi\pi$ bonds between the i and j atoms; r_{ij} is the distance between the i and j atoms; r_o^σ , r_o^π , and $r_o^{\pi\pi}$ are the associated bond radii; and p_{bo} are empirical constants that will be determined from ab-initio simulations or experiments. The energy terms in Eq. (14) are then formulated as a function of the bond-order parameter (see ref. ⁹³ for details).

ReaxFF studies on 2D materials were initiated from studies of various aspects of graphene¹⁰⁸ and inspired investigations for a number of other 2D materials, which are elaborated below.

Graphene—Effect of the environment's chemistry on properties and responses of graphene has been investigated using ReaxFF. For example, effect of oxygen on the mechanical response of graphene¹⁰⁹, effect of the addition of fluorine and hydrogen¹¹⁰ on the structural quality of graphene, as well as the Ni-catalyzed growth process of single-layer graphene¹¹¹, are investigated. The growth mechanism involves atomic deposition and segregation of

C atoms on the Ni substrate, forming dome-like carbon nanotube cap and polygonal ring patterns via atoms→chains→graphene-like layer formation (Fig. 1a). The ReaxFF has also been applied to study reactive events at the graphene–water interface (Fig. 1b)¹¹² and selective desalination via the bare and hydrogenated graphene nanopore¹¹³.

Silicene and phosphorene—Silicene and black phosphorene (BP) are the silicon and phosphorus analogs of graphene, respectively. A favorable route for silicene formation has been proposed by employing the graphene bilayer as a template (Fig. 1c)¹¹⁴. It was found that vacancy defects reduce the thermal stability of silicene, where the critical temperature reduces by more than 30%¹¹⁵. A P/H parameter set has been developed for monolayer BP¹¹⁴ to examine the mechanical, thermal, and chemical stability of both pristine and defective BP.

Molybdenum disulfide—The ReaxFF potential for 2D MoS₂ systems was introduced in ref. 6. This potential could precisely calculate the formation energy of ripplocations in MoS₂ (Fig. 1d)¹¹⁶, which result from the slippage of the upper layer against the lower layer to relax the strain without breaking covalent bonds. This potential was also trained over the vacancy formation energies, diffusion barriers, bending rigidity, and kinetics. It has

also been applied to design S vacancy defects on MoS₂ surface¹¹⁷. Reactive MD simulations have also been used to model the synthesis of MoS₂ layers via sulfidation of MoO₃ surfaces⁷. These simulations identified a three-step reaction pathway as follows: (i) evolution of O₂ and reduction of MoO₃ surface; (ii) S₂-assisted reduction and formation of SO/SO₂; and (iii) sulfidation of the surface via Mo-S bond formation. The ReaxFF MD simulations have also been employed within a multiscale framework to capture thermal properties of MoS₂¹¹⁸. The predicted thermal conductivity of MoS₂ structures with infinite length (37 ± 3 W/mK) falls within the range of experimental results (34.5–110 W/mK)¹¹⁹.

MXenes—MD simulations with ReaxFF of MXenes revealed that intercalating with potassium cations drastically improves water stability and homogeneity of MXenes, and reduce the self-diffusion coefficient of water by two orders of magnitude¹²⁰. The dynamical response of MXenes with different surface terminations to intercalating ions was studied with DFT calculations and ReaxFF MD simulations¹²¹. Figure 1e compares the interlayer distance of Ti₃C₂(OH)₂ MXene bilayer with and without K⁺ ions. Influence of metal ions intercalation on vibrational properties of water molecules trapped between MXene layers was studied using ReaxFF MD simulations¹²². Widening of the interlayer gap may enable the penetration of molecular reactants such as urea, which decomposes readily and leads to the intercalation of ammonium cations¹²³. ReaxFF simulations were performed for defect formation and homoepitaxial growth of TiC layer on Ti₃C₂ MXene structures¹²⁴.

REBO/AIREBO potentials: The REBO potential (E_{ij}^{REBO}) is a combination of attractive (V_{ij}^A) and repulsive (V_{ij}^R) interactions with certain ratio (b_{ij}), $E_{ij}^{\text{REBO}} = V_{ij}^R + b_{ij}V_{ij}^A$. The bond-order interaction ratio, b_{ij} , is dependent on the local coordination in the atomic environment. The REBO potential can define the conjugation of bonds using b_{ij} , and therefore the potential has been widely used for modeling hydrocarbon systems¹²⁵. The repulsive term is expressed by the Brenner equation⁹⁰,

$$V_{ij}^R = w_{ij}(r_{ij}) \left[1 + \frac{Q_{ij}}{r_{ij}} \right] A_{ij} e^{-a_{ij}r_{ij}}. \quad (16)$$

Here, the Q_{ij} , r_{ij} , and a_{ij} parameters depend on i and j . The bond weighting parameter $w_{ij}(r_{ij})$ depends on switching function $S(t)$ as

$$w_{ij}(r_{ij}) = S(t_c(r_{ij})), \quad (17)$$

$$S(t) = \Theta(-t) + \Theta(t)\Theta(1-t)0.5[1 + \cos(\pi t)], \quad (18)$$

$$t_c(r_{ij}) = \frac{r_{ij} - r_{ij}^{\text{min}}}{r_{ij}^{\text{max}} - r_{ij}^{\text{min}}}. \quad (19)$$

The attractive interaction is expressed as

$$V_{ij}^A = -w_{ij}(r_{ij}) \sum_{n=1}^3 B_{ij}^{(n)} e^{B_{ij}^{(n)} r_{ij}}; \quad (20)$$

the bond-order interaction ratio b_{ij} is

$$b_{ij} = \frac{1}{2} [p_{ij}^{\text{on}} + p_{ij}^{\text{off}}] + \pi_{ij}^c + \pi_{ij}^{\text{dh}}. \quad (21)$$

Here, p_{ij}^{on} and p_{ij}^{off} are not necessarily equal as they depend on the penalty function (g_i) of bond angle θ_{jik} between the vector r_{ij} , and vector r_{kir} i.e.,

$$p_{ij}^{\text{on}} = \left[1 + \sum_{k \neq i, j} w_{ik}(r_{ik}) g_i(\cos \theta_{jik}) e^{\lambda_{ijk}} + P_{ij} \right]^{-1/2}. \quad (22)$$

The AIREBO potential is the modification over the REBO potential, which also considers the torsional (E_{kij}^{TORSION}) and LJ (E_{ij}^{LJ}) interactions. The integration of pairwise interactions in AIREBO potential can be represented by the following equation

$$E = \frac{1}{2} \sum_i \sum_{j \neq i} \left[E_{ij}^{\text{REBO}} + E_{ij}^{\text{LJ}} + \sum_{k \neq i, j} \sum_{l \neq i, j, k} E_{kijl}^{\text{TORSION}} \right]. \quad (23)$$

The REBO potential can describe the breaking, formation, and hybridization of covalent bonds. The REBO and AIREBO potentials have been used to study the growth of 2D amorphous carbon, mechanical properties of MoS₂, and even thermal stabilities of C₆₀ 2D nanostructures using atomic coordination, internal stress, and mass density analysis¹²⁶. The subplantation phenomenon during CVD, i.e., penetration of the substrate bulk carbon by carbon atoms, can be explained by this REBO potential. REBO potential is also suitable for modeling and analysis of TMD materials such as MoS₂. The potential results in stabilized structure and good agreement of the structural and mechanical properties^{97,127,128}. It was also used for modeling the synthesis of diamane from graphene and its stability under different conditions¹²⁹.

COMB3 potential: The general formation of the COMB3 potential can be expressed as⁹²

$$U^{\text{tot}}[\{q\}, \{r\}] = U^{\text{es}}[\{q\}, \{r\}] + U^{\text{short}}[\{q\}, \{r\}] + U^{\text{vdW}}[\{q\}, \{r\}] + U^{\text{corr}}[\{q\}, \{r\}] \quad (24)$$

The total potential energy consists of electrostatic energy ($U^{\text{es}}[\{q\}, \{r\}]$), short-range interactions ($U^{\text{short}}[\{q\}, \{r\}]$), long-range vdW interaction ($U^{\text{vdW}}[\{q\}, \{r\}]$), and the correction terms. Here, q and r represent the charge and coordinate array of the elements. The electrostatic energies ($U^{\text{es}}[\{q\}, \{r\}]$) can be represented as

$$U^{\text{es}}[\{q\}, \{r\}] = U^{\text{self}}[\{q\}, \{r\}] + U^{\text{aq}}[\{q\}, \{r\}] + U^{\text{qz}}[\{q\}, \{r\}] + U^{\text{polar}}[\{q\}, \{r\}] \quad (25)$$

The self-interaction energy ($U^{\text{self}}[\{q\}, \{r\}]$) consists of field-effect and ionization energy, or the affinity energy. Charge-to-charge interaction ($U^{\text{aq}}[\{q1s\}, \{r\}]$) is associated with the charge density distribution functions. Nuclear-charge interaction $U^{\text{qz}}[\{q\}, \{r\}]$ depends on the coulombic interaction between charge density distributions in the system. Polar interaction energy $U^{\text{polar}}[\{q\}, \{r\}]$ depends on the charge interactions and dipole distributions in response to the external electric field.

The charge-dependent short-range interaction in Eq. (24) is associated with bond distance functions of the atom and the associated charge functions. This energy term can be expressed by

$$U^{\text{short}}[\{q\}, \{r\}] = \sum_i \sum_{j>i} V_{ij}^{\text{bond}} = \sum_i \sum_{j>i} \{F_c(r_{ij})[V^R(r_{ij}, q_i, q_j)] - b_{ij}V^A(r_{ij}, q_i, q_j)\} \quad (26)$$

Here, V_{ij}^{bond} is the bond energy that is associated with pairwise attraction ($V^A(r_{ij}, q_i, q_j)$) and pairwise repulsion energy ($V^R(r_{ij}, q_i, q_j)$). They exponentially decrease with the interatomic distance r_{ij} . $F_c(r_{ij})$ is the cutoff function.

The long-range interaction energy is defined by the vdW interaction, which can be expressed by the LJ interaction formula¹³⁰

$$U^{\text{S}}[\{q\}, \{r\}] = \sum_i \sum_{j>i}^{NN} 4\epsilon_{ij}^{\text{vdW}} \left[\left(\frac{\sigma_{ij}^{\text{vdW}}}{r_{ij}} \right)^{12} - \left(\frac{\sigma_{ij}^{\text{vdW}}}{r_{ij}} \right)^6 \right] \quad (27)$$

Here, σ_{ij}^{vdW} and $\varepsilon_{ij}^{\text{vdW}}$ are the equilibrium distance and interaction energy, respectively; r_{ij} is the cutoff radii where the interaction assumes zero.

The correction factor in Eq. (24) adjusts the energy penalties associated with specified angles. It can be calculated by a sixth-order Legendre polynomial and bond bending term.

$$U^{\theta}[\{q\}, \{r\}] = \sum_i \sum_{j>i} \sum_{k \neq i} \left\{ \sum_{n=1}^6 K_{ijk}^{LPn} (\cos(\theta_{ijk})) + K_{ijk}^{BB} [\cos(\theta_{ijk}) - \cos(K_{ijk}^{\theta})]^2 \right\} \quad (28)$$

Here, K_{ijk}^{θ} indicates the specific bond angles and θ_{ijk} is the bond angle.

The COMB3 potential has been introduced to study the CVD process for various 2D materials. The charge-optimized COMB3 potentials have been used to simulate the experimental CVD deposition and growth of graphene on metal substrates. Especially, the introduction of dihedral interaction terms in the COMB3 potential can capture the delocalized bonding and bond bending during the CVD process on a particular substrate. The wrinkle formation due to the size mismatch of graphene and Cu-substrate has been studied using COMB3 potential, which was comparable to experimental results⁹⁸. This potential was also used to understand the role of growth parameters such as absorption energy, migration barrier, and temperature in the Cu deposition on ZnO substrate¹³¹. COMB3 potential has also been used to investigate the effect of surface hydroxylation of amorphous SiO₂ substrate on heat conduction of supported graphene¹³².

MESOSCALE SIMULATIONS

Phase-field model

At mesoscale, a simple and effective model for 2D materials growth is the classical Burton-Cabrera-Frank (BCF) theory¹³³, where the island growth is realized by the deposition of adatoms from the supersaturated gas atmosphere and the incorporation of diffusing atoms at the step edge. The direct numerical implementation of the BCF model requires tracking the evolving step edges and applying the boundary conditions due to the sharp-interface nature of the model; in contrast, phase-field diffuse-interface models¹³⁴ avoid the explicit tracking of the interfaces.

The BCF-based phase-field models have been developed since the 1990s for a series of problems related to crystal growth, including collective step motions in a 1-D step train¹³⁵, spiral surface growth during thin-film epitaxy¹³⁶, and step flow under different kinetic regimes¹³⁷. More recently, the combined effects of edge diffusion, the Ehrlich-Schwoebel barrier, deposition, and desorption for epitaxial growth have been investigated in 2-D¹³⁸. Based on these studies, Meca et al.^{139,140} applied the model to the growth of 2D materials with anisotropic diffusion on substrates, using the epitaxial graphene growth on copper foil during CVD as an example, with experimental validations. The typical BCF-based phase-field model for 2D materials growth uses a smoothly varying order parameter ϕ to distinguish the phases, e.g., $\phi = 1$ in the 2D island, $\phi = -1$ in the substrate, and $-1 < \phi < 1$ at step edges. The free energy functional \mathcal{F} of the system has the general form of:

$$\mathcal{F} = \int_V (f(\phi) - \lambda u g(\phi) + \frac{1}{2} W(\theta)^2 |\nabla \phi|^2) dV \quad (29)$$

where the first term $f(\phi)$ is a double-well (or multi-well, e.g., see refs. ^{136,141}) function with global minima at $\phi = 1$ and $\phi = -1$; the second term describes the coupling with the reduced saturation field u , with $g(\phi)$ an interpolation function and λ the coupling coefficient; the third term is the gradient energy due to the inhomogeneous distribution of ϕ at interfaces, where $W(\theta)$ is the

angle-dependent interface thickness with $\theta = \arctan(\phi_y/\phi_x)$. u can be directly related to the adatom concentration c through $u = \Omega(c - c_{eq}^0)$, where c_{eq}^0 is the equilibrium concentration for a flat interface and Ω is the atomic area of the solid phase. The evolution of ϕ is governed by

$$\tau_{\phi} \frac{\partial \phi}{\partial t} = -\frac{\delta \mathcal{F}}{\delta \phi} = -f'(\phi) + \lambda u g'(\phi) + \nabla \cdot (W(\theta)^2 \nabla \phi) - \partial_x (W(\theta) \cdot W'(\theta) \cdot \partial_y \phi) + \partial_y (W(\theta) \cdot W'(\theta) \cdot \partial_x \phi), \quad (30)$$

where τ_{ϕ} is the characteristic time. The evolution of the saturation field u is governed by

$$\frac{\partial u}{\partial t} = D \nabla^2 u + F_d - \frac{u}{\tau_s} - \frac{1}{2} \frac{\partial \phi}{\partial t} \quad (31)$$

where D is the diffusion coefficient, F_d is the effective deposition rate, and τ_s is the characteristic time scale for atom desorption. The phase-field equations (Eqs. (30) and (31)) can recover the sharp-interface BCF model in the limit of $W(\theta) \rightarrow 0$ ¹⁴⁰.

The applications of the phase-field models in 2D materials growth can be categorized into the following three aspects. (1) Reproducing and explaining experimentally observed growth morphologies. Examples include the reconstruction of the spiral growth of SnSe₂¹⁴¹, the verification of impurity-induced bilayered graphene growth¹⁴², and the explanation to island shape change from quasi-hexagons to triangles and dendrite-like morphologies¹⁴³. (2) Investigating the effect of experimental parameters on growth morphologies. Taking the CVD growth of graphene as an example, the effects of flux of carbon species¹⁴⁴, deposition rates¹⁴⁵, and equilibrium saturation¹⁴⁵, and substrate orientation¹³⁹ on graphene island morphologies have been investigated using phase-field simulations, which could provide useful guidance to the experimental control of the growth qualities. (3) Further development of the model to include the effect of additional physical/chemical processes during growth. In addition to the deposition, edge diffusion, and edge anisotropies, phase-field simulations have been extended to model multi-island interactions¹⁴⁶, tilt GB topology of 2D materials on substrates with topological cones¹⁴⁷, and to include the chemical reaction kinetics in the gas phase using a microkinetic model¹⁴⁸. These works improve the fidelity and applicable range of the phase-field model for 2D materials growth.

Nevertheless, a primary obstacle to applying phase-field models for computational synthesis of 2D materials is the lack of connection between the model parameters and the experimentally controllable CVD processing parameters, which is largely due to the difference in size scales of interest. Most of the existing phase-field simulations only focus on the growth of a few 2D islands (up to micrometer scale), which can hardly represent the effect of the macroscopic CVD parameters. One possible solution is to enable the "multiscale" modeling approach⁸, integrating the FEM (see the section on "Macroscale models") to account for the effect of macroscopic CVD parameters on transport phenomena and the mesoscale phase-field model for 2D crystal growth within selected zones of the whole substrate. In particular, the steady-state velocity, concentration, and temperature profiles from FEM can be incorporated in the phase-field model, as it has been proposed and applied by Momeni et al.⁸ (see Fig. 2). The incorporation of chemical reaction kinetics in the phase-field model can improve the accuracy of the predictions and expand its applicability. Phase-field models have also been applied to phase changes in 2D materials. Notable examples include the multi-domain microstructure during H-T' structure transformation in MoTe₂ and the domain switching behaviors under external stimuli¹⁴⁹. A fast Fourier transform algorithm has been implemented to study the domain switching during bending of MoTe₂ (see Fig. 3¹⁴⁹).

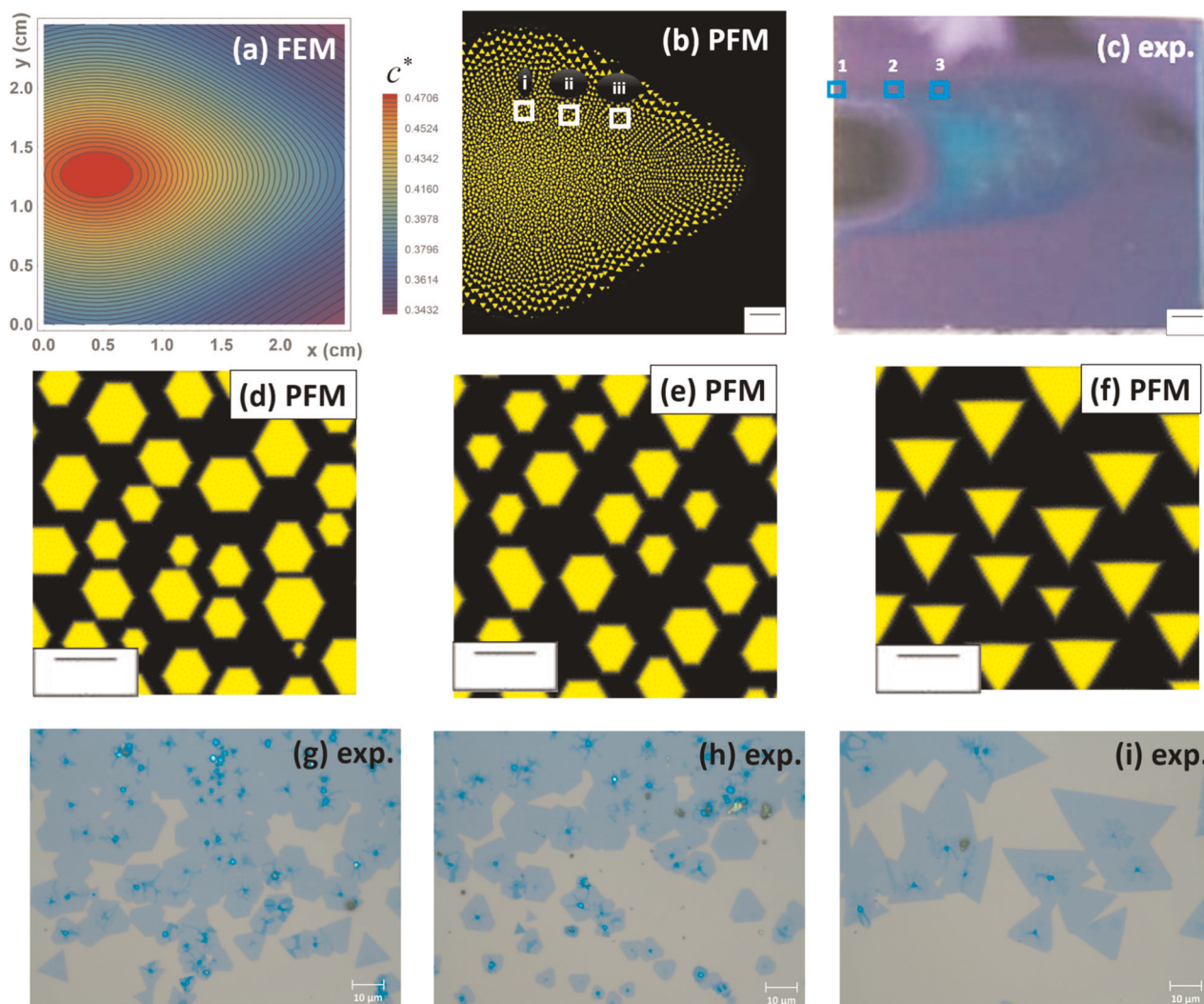


Fig. 2 A coupled macroscale/phase-field simulation and experimental comparison for MoS_2 . **a** Initial precursor concentration distribution from FEM. **b** Phase-field simulation results for MoS_2 morphology on substrate at $t = 0.25$ h, the enlarged images of i–iii boxes are shown in **d–f**. **c** Experimental results for deposition of MoS_2 after deposition for $t = 0.25$ h, the enlarged images of 1–3 boxes are shown in **g, h**. Reprinted from ref. 8 under Creative Commons Attribution 4.0 International License. The scale bar in **a, b** shows $400\ \mu\text{m}$ and the one in **d–f** shows $400\ \mu\text{m}$.

Phase-field-crystal model

Different from the continuous mesoscale phase-field approach, the phase-field-crystal (PFC) approach¹⁵⁰ describes the thermodynamics and dynamics of phase transformations through an atomically varying order parameter related to the atomic density field. With the application of the classical dynamic DFT, PFC can capture the atomistic-scale morphology and evolution dynamics, within diffusional time scales, which is usually challenging for conventional atomistic methods. Recently, PFC has been actively applied to investigate the defect formation and the atomic structure of interfaces, GBs, and triple junctions during the growth of 2D materials¹⁵¹. The unique GB structure and collective domain dynamics in binary 2D materials, e.g., h-BN, was investigated (see Fig. 4¹⁵²).

Compared with the continuous phase-field approach, the advantage of PFC lies in resolving atomistic-scale interface structures and growth dynamics of 2D islands; however, due to the limitation of simulation size, interface dynamics under the effect of realistic CVD parameters are difficult to realize. Future directions of PFC simulations for 2D materials growth include

the consideration of atomistic-scale island-substrate interactions and the integration with the larger-scale phase-field or FEM simulations.

Kinetic Monte Carlo

KMC is another mesoscale technique for predicting the growth morphology and kinetic mechanisms of 2D materials, where all possible kinetic events are listed in an event catalog, and their stochastic sequence are randomly selected based on their activation energies¹⁵³. Activation energies of the related kinetic processes are usually obtained from atomistic-scale calculations. KMC identifies the governing kinetic pathways and simulates the kinetic process. Details of its implementation can be found in ref. 154.

KMC has been extensively applied to simulate the growth of graphene, e.g., the evolution of vacancy complexes and formation of vacancy chains¹⁵⁵, the formation and kinetic effect of multi-member carbon ring complexes¹⁵⁶, etching of graphene GBs due to oxygen migration and reaction¹⁵⁷, and GB evolution following the Stone-Wales mechanism¹⁵⁸. Growth of nanoscale graphene islands

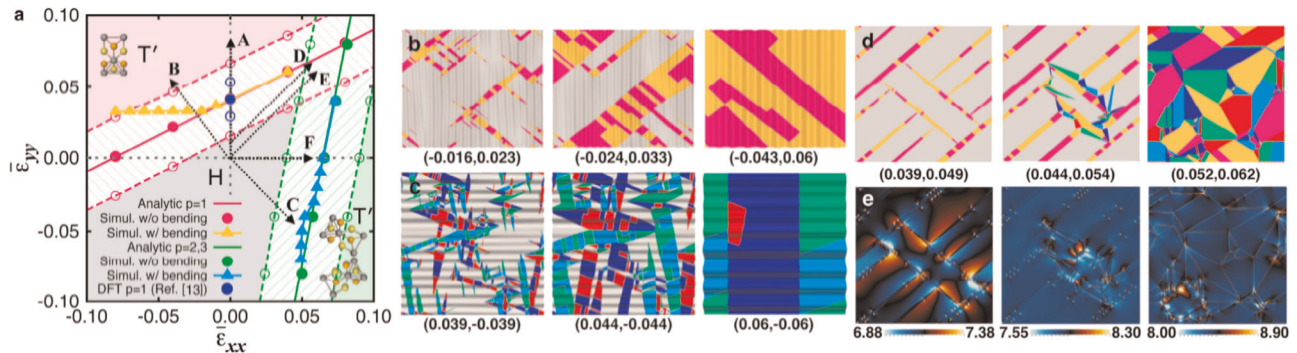


Fig. 3 Variant selection and transformation morphologies in MoTe₂ under an applied in-plane strain $\bar{\epsilon}_{ij}$. **a** Phase diagram in $(\bar{\epsilon}_{xx}, \bar{\epsilon}_{yy})$ space. Colored (hatched) regions correspond to one (two) phase regions. Solid lines (analytic) and filled data points (simulations) indicate the strain at which H and a given T' variant have equal energies. Dashed lines and open symbols similarly represent two-phase coexistence bounds. (\blacktriangle , \triangle) and (\bullet , \circ) correspond to simulations with and without bending, respectively, and blue circles (blue solid circle and blue open circle) represent DFT results at 0. **b–d** Images of the microstructures with increasing time/strain from left to right for strain paths **b–d** in phase diagram **a**. Strain values $(\bar{\epsilon}_{xx}, \bar{\epsilon}_{yy})$ are given below each panel. **e** Corresponding maximum principal stress (GPa) maps for microstructures in **d**. All simulations are for $50 \mu\text{m} \times 50 \mu\text{m}$ simulations. Adapted with permission from ref. ¹⁴⁹. Copyright (2017) American Chemical Society.

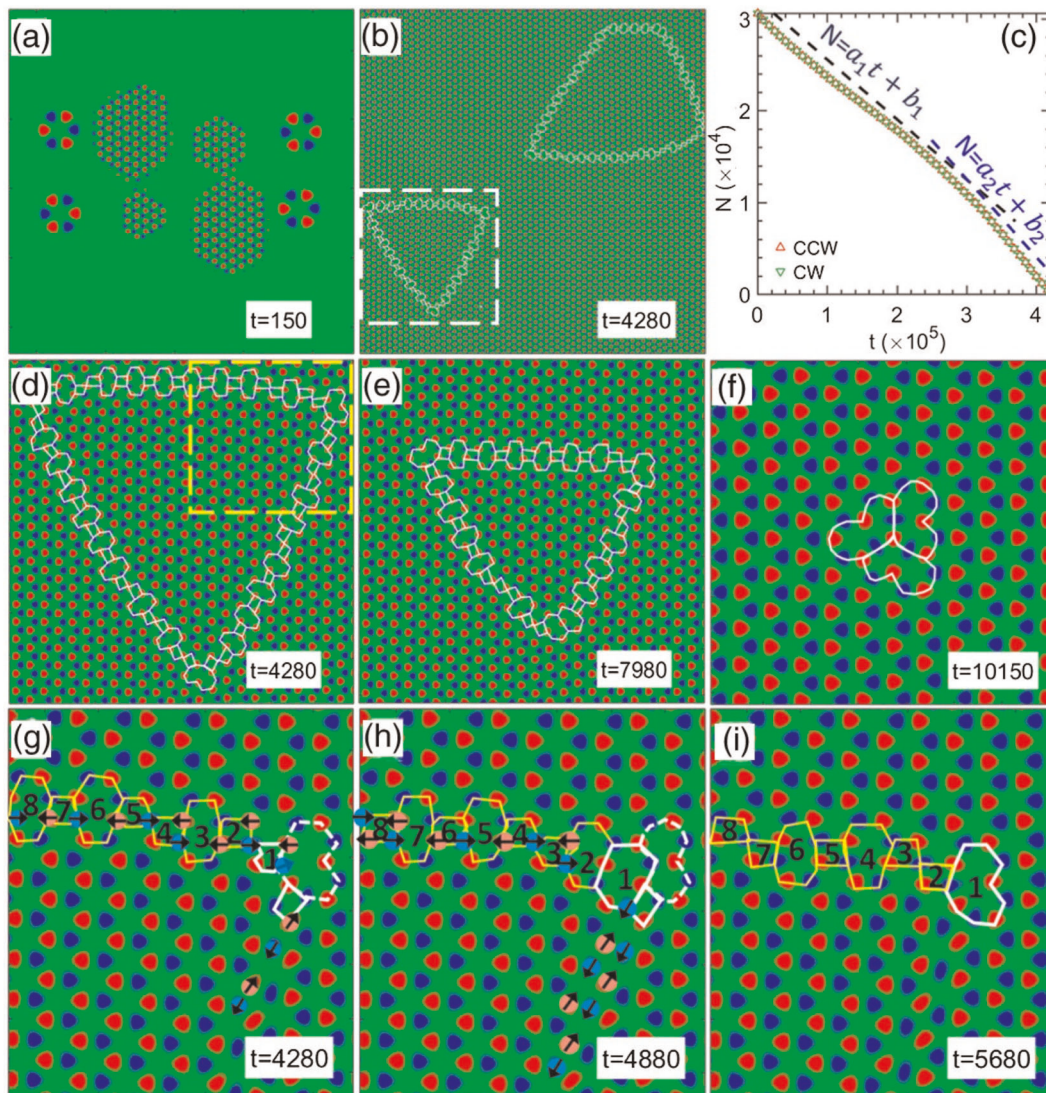


Fig. 4 PFC simulations of the grain growth and coalescence in h-BN. **a–f** Grain coalescence and inversion domain dynamics. **c** Atomic site number N vs. t , showing two regimes $N = -0.065t + 3.045 \times 10^4$ and $N = -0.085t + 3.612 \times 10^4$ via fitting. **d, e** Domain shrinking in the white boxed region of **b**. **f** Transient of three merging heart-shaped defects before their annihilation. **g–i** Time evolution of collective atomic displacements in the yellow boxed corner of **d**. Adapted figure with permission from ref. ¹⁵². Copyright (2017) by the American Physical Society.

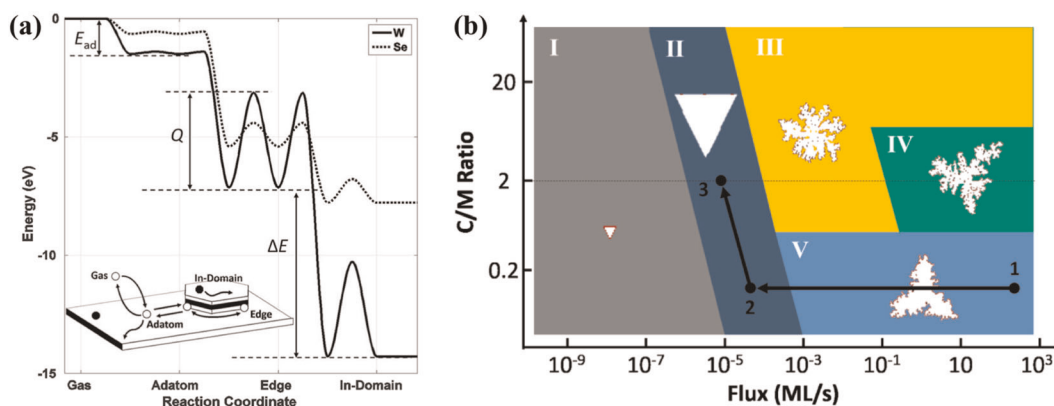


Fig. 5 KMC simulations of WSe_2 growth. **a** Reaction energy diagram of the growth process based on DFT calculations¹⁶⁷. The simulation starts with adatoms. They react with each other to form the TMD domains. After bonded into the domain, the in-flake atoms are mobile through edge diffusion and vacancy diffusion. Each state is defined by its state energy, and each process is defined by its transition activation energy. Adapted from ref. ¹⁵⁴ under Creative Commons Attribution 4.0 International License. **b** Domain morphology diagram on the metal flux-C/M ratio plane at 973 K from KMC simulations. Five regions are identified: I: no growth, II: quasi-equilibrium compact domain, III: fractal, IV: dendrite, and V: semi-compact domain. The arrows show a proposed scenario to obtain high-quality domains with high growth rate. Adapted from ref. ¹⁶⁷.

from carbon monomer nuclei or pre-existing growth fronts has been captured, showing catalytic growth behaviors¹⁵⁹, anisotropic morphological patterns¹⁶⁰, temperature- and deposition-flux-rate-dependent size and shapes¹⁶¹, inhomogeneous and nonlinear growth kinetics due to lattice mismatch¹⁶², and geometry-determined growth mechanisms¹⁶³. The “coastline” graphene morphology during sublimation¹⁶⁴ and the step-flow growth of epitaxial graphene have also been reported¹⁶⁵. Based on KMC simulations for graphene growth on Cu (111) with and without hydrogen, the growth protocol was designed for bilayer growth and N-doped graphene growth¹⁶⁶.

Regarding TMDs, the KMC simulations for the growth of WSe_2 monolayer on graphene have been used to develop the phase diagram of domain morphologies as a function of flux and precursor stoichiometry (Fig. 5)^{154,167}. It was found that the fast kink nucleation and propagation, rather than edge attachment and diffusion, could lead to ultrafast growth of monolayer WSe_2 ¹⁶⁸. KMC simulations also guided CVD growth of large-scale WSe_2 grains by controlling the three-stage adsorption–diffusion–attachment mechanisms¹⁶⁹. KMC model is also a key component in a more generalized mechanistic model for growth morphology predictions of 2D materials⁴⁷.

In summary, the KMC model can be a useful tool for investigating the kinetic pathways and morphologies during the growth of 2D materials. However, the probability-based nature of KMC makes it most suitable for cases where atomic fluctuations are high, i.e., the atomistic and nanoscale morphology and kinetics of 2D materials. For larger-scale simulations, due to the significantly increased system size and the disparate rates of different KMC events, a full-KMC is computationally expensive. As a compromise, multiscale KMC has been developed¹⁶³; simplifications should also be made to account for the key events that are most relevant to the large-scale kinetics¹⁶³. Under such situations, the phase-field approach could be a more efficient option. Meanwhile, the KMC model can provide the governing kinetic mechanisms for phase-field simulations to improve the validity and accuracy of the simulation.

MACROSCALE MODELS

Although the growth of 2D materials occurs at the nano- and mesoscale, it is controlled by physics and parameters that have a macroscopic nature, e.g., heat and mass transfer, furnace

configuration, and gas-phase reactions. Thus, having a thorough understanding of the macroscale physics and processes is essential for controlling the growth of 2D materials and their synthesis by design. We can classify the macroscale models of the growth chamber into four groups: (i) experiment-based models, where rate equations and their constants used to describe the growth¹⁷⁰ are determined from experiments; (ii) analytical models, where the governing equations are simplified and solved analytically¹⁷¹; (iii) adaptive models, where a set of experiments are used to train the model¹⁷²; and (iv) multiphysics models, where the coupled system of governing equations at different length and temporal scales are solved numerically¹⁷³. Among these methods, the last group of models have key advantages, providing a profound understanding to the growth process, flexibility to apply to different growth conditions, and the ability to optimize the process.

A practical macroscale model of the growth chamber should capture the critical governing physics, e.g., the heat and mass transports and chemical reactions. Setting up these models requires several key information that can be obtained from lower scale simulations⁷ or experiments¹⁷⁴. Identifying the gas-phase reactions, we may approximate some of the reaction parameters using classical theories, e.g., the collision rate to estimate the chemisorption rate of species¹⁷⁵ or the group contribution methods to determine the diffusion coefficient¹⁷⁶. The other approximation is for low concentrations of reactive species, where the change in pressure and heat of reaction can be neglected. In the latter case, we may decouple the fluid and heat transfer of gaseous materials from the mass transfer and kinetics. In contrast, for high concentrations of reactive species in the gas phase, such as in metalorganic chemical vapor deposition (MOCVD), the coupled system of equations must be solved¹⁷⁶. A summary of main equations in macroscale models are presented below.

Gas flow

The Navier-Stokes equation governs the flow rates in the growth chamber,

$$\rho \frac{\partial \mathbf{u}}{\partial t} + \rho (\mathbf{u} \cdot \nabla) \mathbf{u} = \nabla \cdot \left[-p \mathbf{I} + \mu (\nabla \mathbf{u} + (\nabla \mathbf{u})^T) \right] + \mathbf{F}; \quad \rho \nabla \cdot \mathbf{u} = 0, \quad (32)$$

where \mathbf{u} is the velocity field, p is pressure, \mathbf{I} is the unit matrix, μ is the dynamic viscosity, and \mathbf{F} is the volumetric applied force, i.e.,

weight. Furthermore, the density ρ is a function of temperature and precursor concentration. In general, the concentration of precursor in the gas phase is low and ρ can be assumed to be only a function of temperature.

Heat transfer

The two main heat transfer mechanisms in the growth chamber are convection and conduction that respectively are

$$Q = \rho C_p \frac{\partial T}{\partial t} + \rho C_p \mathbf{u} \cdot \nabla T + \nabla \cdot \mathbf{q}; \quad \mathbf{q} = -k \nabla T, \quad (33i, ii)$$

where Q is the heat source, C_p is the heat capacity at constant pressure, T is the temperature, \mathbf{q} is the heat flux vector, and k is the thermal conductivity coefficient.

Mass transfer

Commonly, the concentration of precursor materials in the growth chamber is negligible. Thus, the equation governing the mass transfer can be formulated with the flow-assisted diffusion of dilute species

$$R = \frac{\partial c}{\partial t} + \nabla \cdot (-D \nabla c) + \mathbf{u} \cdot \nabla c; \quad N = -D \nabla c + \mathbf{u}c, \quad (34i, ii)$$

where R is the source term for precursor, c is the precursor concentration, D is the diffusion coefficient, and N is the flux of the precursor. Equations (32)–(34) must be solved for a set of initial and boundary conditions, as shown in Table 6.

Chemical reaction

Consider a set of j reactions involving i species of the form $aA + bB + \dots \rightleftharpoons xX + yY + \dots$ with forward and reverse reaction rate constants k_f^j and k_r^j , respectively. These reaction rates depend on the temperature via an Arrhenius expression, e.g., $k_f^j = A_f^j (T/T_{\text{ref}})^n \exp(-E_f^j/R_g T)$. Here, A_f^j denotes the frequency

factor, n the temperature exponent, E_f^j the activation energy, and R_g the gas constant. According to the mass action law, the reaction rates r_j can be described as,

$$r_j = k_f^j \prod_{i \in \text{react}} c_i^{-v_{ij}} - k_r^j \prod_{i \in \text{prod}} c_i^{-v_{ij}}, \quad (35)$$

where c_i is the concentration of i -th species and v_{ij} is the stoichiometric coefficient (negative for reactants and positive for products). The rate equations provide the information regarding the concentration of different species, which in combination with mass and heat balance equations form the complete system of equations.

Macroscale models provide insight into the growth mechanisms and flow regimes, and play a crucial role in determining proper furnace design and growth parameters. Figure 6 shows the application of a macroscopic model of the flow and concentration diffusion in a vertical furnace with a side inlet to study the effect of the gap between the susceptor and substrate. It shows that the presence of the gap results in the formation of eddy currents close to the substrate edge, which disturbs precursor concentration and hinders the formation of 2D materials that is consistent with the experimental observations. These models have been successfully used in determining the mechanisms governing the growth of 2D materials. For example, it was revealed that the concentration gradient of the precursor is a critical factor in determining the growth morphology of 2D materials, where a low concentration gradient along the substrate leads to the formation of multigrain 2D films. In contrast, moderate planar concentration gradients lead to isolated islands of varying morphologies, and an out-of-plane gradient leads to the formation of standing 2D materials^{173,177}. Furthermore, macroscale models can be combined with lower scale models to form a multiscale platform with high fidelity, e.g., ref.⁸.

MATERIALS GENOME APPROACHES

Data-driven methods have been employed to satisfy the urgent need for theoretical development of 2D materials. The improvement of computational power has resulted in extensive collections of data and scientifically organized databases, which can be used by methods such as data mining and machine learning, to accelerate the computational design of new 2D materials.

Database of 2D materials

Compared with the databases of 3D bulk materials such as the Crystallographic Open Database¹⁷⁸, the Inorganic Crystal Structure Database¹⁷⁹, and the Cambridge Crystallographic Data Centre¹⁸⁰, the database focused on 2D materials is still under development. Several 2D materials databases have been attempted primarily based on a high-throughput approach coupled with first-principles and quantum theory to address this shortcoming. Besides, data-mining methods have also been applied to screen those bulk materials databases and identify possible 2D materials from 3D structures. These approaches can provide various information about 2D materials that have been or not been synthesized in experiments. For example, using a criterion to identify 2D materials, a database has been developed on the basis of experimental and DFT data¹⁸¹. This database provides information including exfoliation energy, bandgap, work function, and elastic-constant values of various 2D materials, and also predicted hundreds of new 2D materials for the experimental synthesis. DFT and many-body perturbation theory have been used to generate the Computational 2D Materials Database (C2DB)¹⁸². The C2DB contains structural, thermodynamic, elastic, electronic, magnetic, and optical information of about two thousand 2D materials in more than 30 crystal structures. A few hundred new monolayer structures

Table 6. Common boundary conditions for the heat and mass transfer in macroscale models.	
Navier-Stokes	
No slip on walls	$\mathbf{u} = \mathbf{0}$
Normal inflow velocity ^a	$\mathbf{u} = -U_0 \mathbf{n}$
Laminar inflow ^b	$L_{\text{ent}} \nabla_{\mathbf{t}} \cdot \left[-p\mathbf{I} + \mu \left(\nabla_{\mathbf{t}} \mathbf{u} + (\nabla_{\mathbf{t}} \mathbf{u})^T \right) \right] = -p_{\text{ent}} \mathbf{n}$
Mass Flow ^c	$-\int_{\partial \Omega} \frac{\rho}{P_{\text{st}}} (\mathbf{u} \cdot \mathbf{n}) d_{bc} dS = Q_{\text{scm}}$
Zero outlet pressure	$-p\mathbf{I} + \mu (\nabla \mathbf{u} + (\nabla \mathbf{u})^T) - \frac{2}{3} \mu (\nabla \cdot \mathbf{u}) \mathbf{I} = \mathbf{0}$
Heat transfer	
Inlet	$-\mathbf{n} \cdot \mathbf{q} = \mathbf{0}$
Thermal insulation	$-\mathbf{n} \cdot \mathbf{q} = \mathbf{0}$
Inflow heat flux ^d	$-\mathbf{n} \cdot \mathbf{q} = -q_0 \frac{A(\mathbf{u} \cdot \mathbf{n})}{\int_s \mathbf{u} \cdot \mathbf{n} ds} + \rho (h_{\text{in}} - h_{\text{ext}}) \mathbf{u} \cdot \mathbf{n}$
Wall temperature	$T = T(r)$
Flow-assisted diffusion	
No flux at furnace walls	$-\mathbf{n} \cdot \mathbf{N}_i = \mathbf{0}$
Specified concentration	$c = c_0(r)$
Outflow	$-\mathbf{n} \cdot D_i \nabla c_i$
Inflow	$c = c_{\text{in}}$

^a \mathbf{n} is the unit normal vector of the boundary surface.
^b L_{ent} is the entrance length, and p_{ent} is the entrance pressure.
^c $\rho_{\text{st}} = \frac{P_{\text{st}} M_n}{RT_{\text{st}}}$; M_n is the mean molar mass, and T_{st} and P_{st} are standard temperature and pressure. Q_{scm} is the mass flow in the scm units.
^d A is the surface area and q_0 is the inward heat flux.

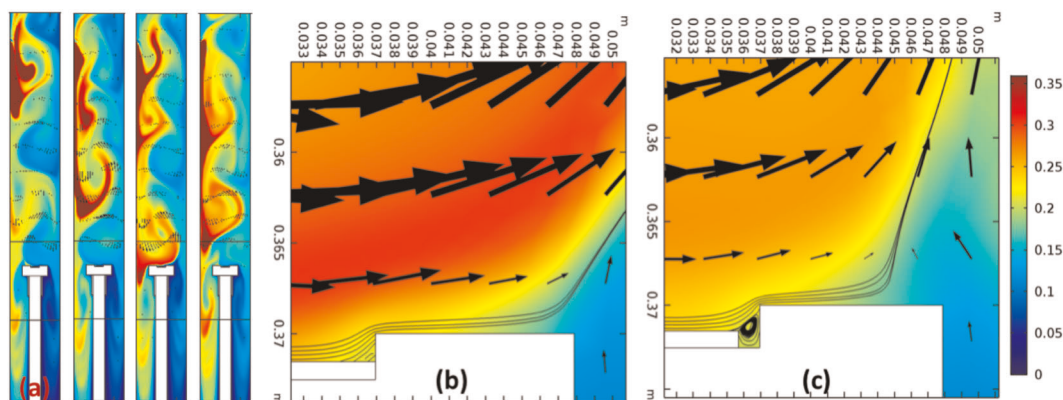


Fig. 6 Macroscale model of the flow and precursor concentration in a vertical MOCVD furnace. **a** Snapshots of the concentration profile within the growth chamber with a heated susceptor where the precursor enters from top left side of the furnace. It indicates the effect of buoyancy forces on inducing instabilities and back flow formation. **b, c** Magnified views of the flow and concentration profiles close to the susceptor/substrate. Eddy current forms when there is a gap between the susceptor and substrate which hinders formation of 2D materials.

that were previously unknown, but potentially synthesizable were also identified. A data-mining method has also been used to screen the bulk materials from the open database and identified a few hundred 2D weakly bonded solid materials¹⁸³. The band gaps and point groups that determine piezoelectric and nonlinear optical properties in these materials were also provided. A search in the database of bulk materials was performed and DFT calculations were used to explore these materials for possible exfoliation, where more than one thousand materials have been identified¹⁴. Information including electronic, vibrational, magnetic and topological properties of promising materials was also provided. Similarly, the crystal database was screened for layered motifs, and hundreds of stable layered materials were found that can be considered as candidates for the formation of 2D monolayers via exfoliation¹⁸⁴.

Machine learning method

Machine learning models trained using 2D material databases can be parameterized, validated, and therefore used for predictive exploration of novel 2D materials with desired properties. Machine learning methods can also aid the understanding of the complex correlations between structures and properties in 2D materials. A combination of machine learning with MD simulations and in-situ high-resolution transmission electron microscopy to explore TMDs has been performed¹⁸⁵, where machine learning provided information for structural optimization and evolution of defects to help understand the structural transition in 2D TMDs. A practical method to explore hybrid 2D materials was developed by coupling machine learning with DFT calculations¹⁸⁶. The structural and electronic properties of different hybrid 2D materials were provided and various parameters for vdW heterostructures were screened. A machine learning model with force-field-inspired descriptors in material screening for complex systems has been introduced and used to discover exfoliated 2D-layered materials¹⁸⁷. An artificial neural network for titanium dioxide systems was trained based on the a DFT calculated database, where a novel quasi 2D titanium dioxide structure was revealed¹⁸⁸. Similarly, new 2D materials with high magnetic moments were found using a machine learning model trained by first-principles data¹⁸⁹. Machine learning methods have also been used to aid the development of force fields for classical simulations of materials¹⁹⁰. For instance, a force field for classical simulations of stanene was developed using a machine learning method trained by data sets from ab-initio results to calculate the mechanical and thermal properties of stanene¹⁹⁰. 2D materials without bulk layered counterparts are also being discovered, using genetic

algorithms^{191,192} or particle swarm optimization, both using energy-based merit criteria and additional biases towards 2D sheets (see refs. ^{17,193,194}).

OUTLOOK

This overview summarizes the state-of-the-art of modeling efforts on the growth of 2D-layered materials and outlines the advantages and limitations of computational models and methods at different length and time scales. The emphasis is on modeling, understanding, and predicting the thermodynamics and kinetics of 2D materials growth. The eventual goal is to develop computational tools and techniques to realize the “synthesis by design” of 2D materials.

An ideal computational model should not only capture accurately the correct physics to allow robust designs but also be computationally efficient to be employed for active control of the growth process. The complex nature of the growth of 2D materials requires applications of a range of models, which operate at multiple length and temporal scales to capture the full range of the growth phenomena from macroscale flow and concentration profiles in the furnace to atomistic reactions leading to formation and growth of 2D materials at mesoscale. Modeling the full spectrum of mechanisms involved in the growth of 2D materials is challenging due to the limitations associated with each of the computational models at different length and temporal scales.

A high-fidelity prediction of 2D materials growth often requires an integration of methods applicable across different scales, ranging from electronic and atomistic, to mesoscale phenomenological, and large-scale continuum models. For example, chemical potentials of different phases and the migration energies of atomic species in different structural and chemical environment from electronic and atomistic models can be employed to parametrize mesoscale phase-field models for predicting the morphology and thus characteristics of as-grown 2D materials with the boundary conditions specified by the information obtained from large-scale continuum models such as temperature distribution in the growth chamber as presented in ref. ⁸. Furthermore, technical obstacles to in-situ experimental monitoring of growth hinder the validation of computational predictions. The current mathematical and numerical models are computationally expensive and commonly do not capture simultaneously all the physics involved in a growth process of 2D materials, limiting their widespread adoption in active control of 2D materials growth. One promising way to circumvent this challenge is to use machine learning models trained using experimental and

computational databases of the 2D materials structure and growth conditions such as the ones available at the 2D Crystal Consortium–Materials Innovation Platform. Finally, the models and approaches applied in understanding the growth of 2D materials can be adapted to the growth of other materials that use the same synthesis techniques, e.g., CVD growth of thin films.

As a future perspective, we can envision two main strategies for the development of computational models and their applications to the design and synthesis of 2D materials, which are long-term challenging goals of the field. First is the open-loop design approach, where the growth chamber design and synthesis conditions are determined by performing a series of simulations mimicking the thermophysical conditions and reaction and growth kinetics that would be expected in experiments. In this approach, the models must have high fidelity and a comprehensive sensitivity analysis should be performed to obtain a robust design. The second approach is the closed-loop design that the developed models will be utilized to determine the states of the system to be passed to a controller which adjusts the growth conditions in real-time. In this approach, the computational efficiency of the models is key to the success of the design.

DATA AVAILABILITY

All data that was obtained during this project are available from the authors.

Received: 2 May 2019; Accepted: 13 February 2020;

Published online: 19 March 2020

REFERENCES

- Henini, M. Principles of electronic materials and devices (second edition). *Microelectron. J.* **33**, 681 (2002).
- Yi, M. & Shen, Z. A review on mechanical exfoliation for the scalable production of graphene. *J. Mater. Chem. A* **3**, 11700–11715 (2015).
- Coleman, J. N. et al. Two-dimensional nanosheets produced by liquid exfoliation of layered materials. *Science* **331**, 568–571 (2011).
- Lim, Y. R. et al. Roll-to-roll production of layer-controlled molybdenum disulfide: a platform for 2D semiconductor-based industrial applications. *Adv. Mater.* **30**, 1705270 (2018).
- McKee, G. S. B. & Vecchio, K. S. Thermogravimetric analysis of synthesis variation effects on CVD generated multiwalled carbon nanotubes. *J. Phys. Chem. B* **110**, 1179–1186 (2006).
- Ostadhosse, A. et al. ReaxFF reactive force-field study of molybdenum disulfide (MoS₂). *J. Phys. Chem. Lett.* **8**, 631–640 (2017).
- Hong, S. et al. Computational synthesis of MoS layers by reactive molecular dynamics simulations: initial sulfidation of MoO surfaces. *Nano Lett.* **17**, 4866–4872 (2017).
- Momeni, K., Ji, Y., Zhang, K., Robinson, J. A. & Chen, L.-Q. *Multiscale Framew. Simul.-Guide. growth 2D Mater. npj 2D Mater. Appl.* **2**, 27 (2018).
- Zhang, X. et al. Defect-controlled nucleation and orientation of WSe₂ on hBN: a route to single-crystal epitaxial monolayers. *ACS Nano* **13**, 3341–3352 (2019).
- Chen, W., Gui, X., Yang, L., Zhu, H. & Tang, Z. Wrinkling of two-dimensional materials: methods, properties and applications. *Nanoscale Horiz.* **4**, 291–320 (2019).
- Momeni, K. & Levitas, V. I. Propagating phase interface with intermediate interfacial phase: phase field approach. *Phys. Rev. B* **89** (2014).
- Mehdipour, H. & Ostrikov, K. Kinetics of low-pressure, low-temperature graphene growth: toward single-layer, single-crystalline structure. *ACS Nano* **6**, 10276–10286 (2012).
- Jiang, J.-W., Wang, B.-S., Wang, J.-S. & Park, H. S. A review on the flexural mode of graphene: lattice dynamics, thermal conduction, thermal expansion, elasticity and nanomechanical resonance. *J. Phys. Condens. Matter* **27**, 83001 (2015).
- Mounet, N. et al. Two-dimensional materials from high-throughput computational exfoliation of experimentally known compounds. *Nat. Nanotechnol.* **13**, 246–252 (2018).
- Zhuang, H. L. & Hennig, R. G. Stability and magnetism of strongly correlated single-layer VS₂. *Phys. Rev. B* **93**, 54429 (2016).
- Cohen, A. J., Mori-Sánchez, P. & Yang, W. Insights into current limitations of density functional theory. *Science* **321**, 792–794 (2008).
- Paul, J. T. et al. Computational methods for 2D materials: discovery, property characterization, and application design. *J. Phys. Condens. Matter* **29**, 473001 (2017).
- Sun, Y. et al. Low-temperature solution synthesis of few-layer 1T'-MoTe₂ nanostructures exhibiting lattice compression. *Angew. Chem. Int. Ed.* **55**, 2830–2834 (2016).
- Kretschmer, S., Komsa, H.-P., Bøggild, P. & Krasheninnikov, A. V. Structural transformations in two-dimensional transition-metal dichalcogenide MoS₂ under an electron beam: insights from first-principles calculations. *J. Phys. Chem. Lett.* **8**, 3061–3067 (2017).
- Duerloo, K.-A. N., Li, Y. & Reed, E. J. Structural phase transitions in two-dimensional Mo- and W-dichalcogenide monolayers. *Nat. Commun.* **5**, 4214 (2014).
- Gan, L.-Y., Zhang, Q., Zhao, Y.-J., Cheng, Y. & Schwingschlögl, U. Order-disorder phase transitions in the two-dimensional semiconducting transition metal dichalcogenide alloys Mo_{1-x}W_xX₂ (X = S, Se, and Te). *Sci. Rep.* **4**, 6691 (2015).
- Komsa, H.-P. & Krasheninnikov, A. V. Two-dimensional transition metal dichalcogenide alloys: stability and electronic properties. *J. Phys. Chem. Lett.* **3**, 3652–3656 (2012).
- Dumcenco, D. O., Kobayashi, H., Liu, Z., Huang, Y.-S. & Suenaga, K. Visualization and quantification of transition metal atomic mixing in Mo_{1-x}W_xS₂ single layers. *Nat. Commun.* **4**, 1351 (2013).
- Azizi, A. et al. Spontaneous formation of atomically thin stripes in transition metal dichalcogenide monolayers. *Nano Lett.* **16**, 6982–6987 (2016).
- Grimme, S., Antony, J., Ehrlich, S. & Krieg, H. A consistent and accurate ab initio parametrization of density functional dispersion correction (DFT-D) for the 94 elements H-Pu. *J. Chem. Phys.* **132**, 154104 (2010).
- Tkatchenko, A. & Scheffler, M. Accurate molecular van der Waals interactions from ground-state electron density and free-atom reference data. *Phys. Rev. Lett.* **102**, 73005 (2009).
- Dion, M., Rydberg, H., Schröder, E., Langreth, D. C. & Lundqvist, B. I. Van der Waals density functional for general geometries. *Phys. Rev. Lett.* **92**, 246401 (2004).
- He, J., Hummer, K. & Franchini, C. Stacking effects on the electronic and optical properties of bilayer transition metal dichalcogenides MoS₂, MoSe₂, WS₂, and WSe₂. *Phys. Rev. B* **89**, 75409 (2014).
- Dreyer, C. E., Janotti, A. & Van de Walle, C. G. Absolute surface energies of polar and nonpolar planes of GaN. *Phys. Rev. B* **89**, 81305 (2014).
- Mathew, K. et al. MPIInterfaces: A Materials Project based Python tool for high-throughput computational screening of interfacial systems. *Comput. Mater. Sci.* **122**, 183–190 (2016).
- Henkelman, G., Uberuaga, B. P. & Jonsson, H. A climbing image nudged elastic band method for finding saddle points and minimum energy paths. *J. Chem. Phys.* **113**, 9901–9904 (2000).
- Eichfeld, S. M., Colon, V. O., Nie, Y., Cho, K. & Robinson, J. A. Controlling nucleation of monolayer WSe₂ during metal-organic chemical vapor deposition growth. *2D Mater.* **3**, 25015 (2016).
- Tuckerman, M. E. *Statistical mechanics: theory and molecular simulation* (Oxford Univ. Press, 2010).
- Bucko, T. Ab initio calculations of free-energy reaction barriers. *J. Phys. Condens. Matter* **20**, 64211 (2008).
- Sheppard, D., Terrell, R. & Henkelman, G. Optimization methods for finding minimum energy paths. *J. Chem. Phys.* **128**, 134106 (2008).
- Misawa, M. et al. Reactivity of sulfur molecules on MoO₃ (010) surface. *J. Phys. Chem. Lett.* **8**, 6206–6210 (2017).
- Torrie, G. M. & Valleau, J. P. Nonphysical sampling distributions in Monte Carlo free-energy estimation: umbrella sampling. *J. Comput. Phys.* **23**, 187–199 (1977).
- Sun, H. et al. Theory of thin-film-mediated exfoliation of van der Waals bonded layered materials. *Phys. Rev. Mater.* **2**, 94004 (2018).
- van Erp, T. S. & Bolhuis, P. G. Elaborating transition interface sampling methods. *J. Comput. Phys.* **205**, 157–181 (2005).
- Laio, A. & Parrinello, M. Escaping free-energy minima. *Proc. Natl Acad. Sci. USA* **99**, 12562–12566 (2002).
- Darve, E. & Pohorille, A. Calculating free energies using average force. *J. Chem. Phys.* **115**, 9169–9183 (2001).
- Kaminski, J. W., Kratzer, P. & Ratsch, C. Towards a standardized setup for surface energy calculations. *Phys. Rev. B* **95**, 85408 (2017).
- Liu, Y., Bhowmick, S. & Yakobson, B. I. BN white graphene with 'colorful' edges: the energies and morphology. *Nano Lett.* **11**, 3113–3116 (2011).
- Chetty, N. & Martin, R. M. First-principles energy density and its applications to selected polar surfaces. *Phys. Rev. B* **45**, 6074–6088 (1992).

45. Artyukhov, V. I., Liu, Y. & Yakobson, B. I. Equilibrium at the edge and atomistic mechanisms of graphene growth. *Proc. Natl Acad. Sci. USA* **109**, 15136–15140 (2012).
46. Li, X. et al. Edge-controlled growth and etching of two-dimensional GaSe monolayers. *J. Am. Chem. Soc.* **139**, 482–491 (2017).
47. Rajan, A. G., Warner, J. H., Blankschtein, D. & Strano, M. S. Generalized mechanistic model for the chemical vapor deposition of 2D transition metal dichalcogenide monolayers. *ACS Nano* **10**, 4330–4344 (2016).
48. Freysoldt, C. et al. First-principles calculations for point defects in solids. *Rev. Mod. Phys.* **86**, 253–305 (2014).
49. Stone, A. J. & Wales, D. J. Theoretical studies of icosahedral C₆₀ and some related species. *Chem. Phys. Lett.* **128**, 501–503 (1986).
50. Komsa, H. P., Berseneva, N., Krasheninnikov, A. V. & Nieminen, R. M. Charged point defects in the flatland: Accurate formation energy calculations in two-dimensional materials. *Phys. Rev. X* **4**, 31044 (2014).
51. Rao, R. et al. Dynamics of cleaning, passivating and doping monolayer MoS₂ by controlled laser irradiation. *2D Mater.* **6**, 45031 (2019).
52. Rastogi, P., Kumar, S., Bhowmick, S., Agarwal, A. & Chauhan, Y. S. Doping strategies for monolayer MoS₂ via surface adsorption: a systematic study. *J. Phys. Chem. C* **118**, 30309–30314 (2014).
53. Weston, L., Wickramaratne, D., Mackoite, M., Alkauskas, A. & Van de Walle, C. G. Native point defects and impurities in hexagonal boron nitride. *Phys. Rev. B* **97**, 214104 (2018).
54. Walsh, A. & Zunger, A. Instilling defect tolerance in new compounds. *Nat. Mater.* **16**, 964–967 (2017).
55. Zhang, F. et al. Full orientation control of epitaxial MoS₂ on hBN assisted by substrate defects. *Phys. Rev. B* **99**, 155430 (2019).
56. Lee, G.-D. et al. Diffusion, coalescence, and reconstruction of vacancy defects in graphene layers. *Phys. Rev. Lett.* **95**, 205501 (2005).
57. Kotakoski, J., Krasheninnikov, A. V. & Nordlund, K. Energetics, structure, and long-range interaction of vacancy-type defects in carbon nanotubes: atomistic simulations. *Phys. Rev. B* **74**, 245420 (2006).
58. Momeni, K., Attariani, H. & Lesar, R. A. Structural transformation in monolayer materials: A 2D to 1D transformation. *Phys. Chem. Chem. Phys.* **18**, 19873–19879 (2016).
59. Zhou, W. et al. Intrinsic structural defects in monolayer molybdenum disulfide. *Nano Lett.* **13**, 2615–2622 (2013).
60. Zou, X., Liu, Y. & Yakobson, B. I. Predicting dislocations and grain boundaries in two-dimensional metal-disulfides from the first principles. *Nano Lett.* **13**, 253–258 (2013).
61. Xu, F., Yu, H., Sadrzadeh, A. & Yakobson, B. I. Riemann surfaces of carbon as graphene nanosolenoids. *Nano Lett.* **16**, 34–39 (2016).
62. Yu, Z. G., Zhang, Y.-W. & Yakobson, B. I. An anomalous formation pathway for dislocation-sulfur vacancy complexes in polycrystalline monolayer MoS₂. *Nano Lett.* **15**, 6855–6861 (2015).
63. Sha, Z. D. et al. Inverse pseudo Hall-Petch relation in polycrystalline graphene. *Sci. Rep.* **4**, 5991 (2014).
64. Grantab, R., Shenoy, V. B. & Ruoff, R. S. Anomalous strength characteristics of tilt grain boundaries in graphene. *Science* **330**, 946–948 (2010).
65. Zhang, Z., Yang, Y., Xu, F., Wang, L. & Yakobson, B. I. Unraveling the sinusoidal grain boundaries in graphene. *Adv. Funct. Mater.* **25**, 367–373 (2015).
66. Liu, Y., Xu, F., Zhang, Z., Penev, E. S. & Yakobson, B. I. Two-dimensional mono-elemental semiconductor with electronically inactive defects: the case of phosphorus. *Nano Lett.* **14**, 6782–6786 (2014).
67. Jones, J. E. On the determination of molecular fields. II. From the equation of state of a gas. *Proc. R. Soc. Lond. Ser. A Math. Phys. Eng. Sci.* **106**, 463–477 (1924).
68. Wen, M., Carr, S., Fang, S., Kaxiras, E. & Tadmor, E. B. Dihedral-angle-corrected registry-dependent interlayer potential for multilayer graphene structures. *Phys. Rev. B* **98**, 235404 (2018).
69. Kolmogorov, A. N. & Crespi, V. H. Registry-dependent interlayer potential for graphitic systems. *Phys. Rev. B* **71**, 235415 (2005).
70. Naik, M. H., Maity, I., Maiti, P. K. & Jain, M. Kolmogorov–Crespi potential for multilayer transition-metal dichalcogenides: capturing structural transformations in Moiré superlattices. *J. Phys. Chem. C* **123**, 9770–9778 (2019).
71. Rappe, A. K., Casewit, C. J., Colwell, K. S., Goddard, W. A. & Skiff, W. M. UFF, a full periodic table force field for molecular mechanics and molecular dynamics simulations. *J. Am. Chem. Soc.* **114**, 10024–10035 (1992).
72. Stillinger, F. H. & Weber, T. A. Computer simulation of local order in condensed phases of silicon. *Phys. Rev. B* **31**, 5262–5271 (1985).
73. Jiang, J.-W. Parameterization of Stillinger–Weber potential based on valence force field model: application to single-layer MoS₂ and black phosphorus. *Nanotechnology* **26**, 315706 (2015).
74. Jiang, J.-W., Park, H. S. & Rabczuk, T. Molecular dynamics simulations of single-layer molybdenum disulfide (MoS₂): Stillinger–Weber parameterization, mechanical properties, and thermal conductivity. *J. Appl. Phys.* **114**, 64307–64311 (2013).
75. Jiang, J.-W., Qi, Z., Park, H. S. & Rabczuk, T. Elastic bending modulus of single-layer molybdenum disulfide (MoS₂): finite thickness effect. *Nanotechnology* **24**, 435705 (2013).
76. Yapicioglu, H., Kandemir, A., Sevik, C., Çağın, T. & Kinaci, A. Thermal transport properties of MoS₂ and MoSe₂ monolayers. *Nanotechnology* **27**, 55703 (2016).
77. Norouzzadeh, P. & Singh, D. J. Thermal conductivity of single-layer WSe₂ by a Stillinger–Weber potential. *Nanotechnology* **28**, 75708 (2017).
78. Jiang, J.-W., Rabczuk, T. & Park, H. S. A Stillinger–Weber potential for single-layered black phosphorus, and the importance of cross-pucker interactions for a negative Poisson's ratio and edge stress-induced bending. *Nanoscale* **7**, 6059–6068 (2015).
79. Xu, W., Zhu, L., Cai, Y., Zhang, G. & Li, B. Direction dependent thermal conductivity of monolayer phosphorene: parameterization of Stillinger–Weber potential and molecular dynamics study. *J. Appl. Phys.* **117**, 214308 (2015).
80. Jiang, J.-W. & Zhou, Y.-P. In *Parameterization of Stillinger–Weber Potential for Two-Dimensional Atomic Crystal* Chapter 1 (IntechOpen, 2017). <https://doi.org/10.5772/intechopen.71929>.
81. Allinger, N. L., Yuh, Y. H. & Lii, J. H. Molecular mechanics. The MM3 force field for hydrocarbons. 1. *J. Am. Chem. Soc.* **111**, 8551–8566 (1989).
82. Sun, H. COMPASS: an ab initio force-field optimized for condensed-phase applications overview with details on alkane and benzene compounds. *J. Phys. Chem. B* **102**, 7338–7364 (1998).
83. Keating, P. N. Effect of invariance requirements on the elastic strain energy of crystals with application to the diamond structure. *Phys. Rev.* **145**, 637–645 (1966).
84. Allinger, N. L. Calculation of molecular structure and energy by force-field methods. *Adv. Phys. Org. Chem.* **13**, 1–82 (1976).
85. Allinger, N. L. Conformational analysis. 130. MM2. A hydrocarbon force field utilizing V1 and V2 torsional terms. *J. Am. Chem. Soc.* **99**, 8127–8134 (1977).
86. Allinger, N. L., Chen, K., Katzenellenbogen, J. A., Wilson, S. R. & Anstead, G. M. Hyperconjugative effects on carbon–carbon bond lengths in molecular mechanics (MM4). *J. Comput. Chem.* **17**, 747–755 (1996).
87. Tu, Z. & Ou-Yang, Z. Single-walled and multiwalled carbon nanotubes viewed as elastic tubes with the effective Young's moduli dependent on layer number. *Phys. Rev. B* **65**, 233407 (2002).
88. Chang, T. & Gao, H. Size-dependent elastic properties of a single-walled carbon nanotube via a molecular mechanics model. *J. Mech. Phys. Solids* **51**, 1059–1074 (2003).
89. Tersoff, J. Empirical interatomic potential for carbon, with applications to amorphous carbon. *Phys. Rev. Lett.* **61**, 2879–2882 (1988).
90. Brenner, D. W. et al. A second-generation reactive empirical bond order (REBO) potential energy expression for hydrocarbons. *J. Phys. Condens. Matter* **14**, 783–802 (2002).
91. Stuart, S. J., Tutein, A. B. & Harrison, J. A. A reactive potential for hydrocarbons with intermolecular interactions. *J. Chem. Phys.* **112**, 6472–6486 (2000).
92. Liang, T., Devine, B., Phillpot, S. R. & Sinnott, S. B. Variable charge reactive potential for hydrocarbons to simulate organic-copper interactions. *J. Phys. Chem. A* **116**, 7976–7991 (2012).
93. Van Duin, A. C. T., Dasgupta, S., Lorant, F. & Goddard, W. A. ReaxFF: a reactive force field for hydrocarbons. *J. Phys. Chem. A* **105**, 9396–9409 (2001).
94. Liang, T. et al. Reactive potentials for advanced atomistic simulations. *Annu. Rev. Mater. Res.* **43**, 109–129 (2013).
95. Fonseca, A. F. et al. Graphene–titanium interfaces from molecular dynamics simulations. *ACS Appl. Mater. Interfaces* **9**, 33288–33297 (2017).
96. Mortazavi, B., Pereira, L. F. C., Jiang, J.-W. & Rabczuk, T. Modelling heat conduction in polycrystalline hexagonal boron-nitride films. *Sci. Rep.* **5**, 13228 (2015).
97. Mukhopadhyay, T., Mahata, A., Adhikari, S. & Asle Zaeem, M. Probing the shear modulus of two-dimensional multiplanar nanostructures and heterostructures. *Nanoscale* **10**, 5280–5294 (2018).
98. Klaver, T. P. C., Zhu, S.-E., Sluiter, M. H. F. & Janssen, G. C. A. M. Molecular dynamics simulation of graphene on Cu (100) and (111) surfaces. *Carbon N. Y.* **82**, 538–547 (2015).
99. Hong, S. et al. Chemical vapor deposition synthesis of MoS₂ layers from the direct sulfidation of MoO₃ surfaces using reactive molecular dynamics simulations. *J. Phys. Chem. C* **122**, 7494–7503 (2018).
100. Tersoff, J. New empirical model for the structural properties of silicon. *Phys. Rev. Lett.* **56**, 632–635 (1986).
101. Tersoff, J. New empirical approach for the structure and energy of covalent systems. *Phys. Rev. B* **37**, 6991–7000 (1988).
102. Jiang, J.-W. & Wang, J.-S. Manipulation of heat current by the interface between graphene and white graphene. *Europhys. Lett.* **96**, 16003 (2011).
103. Mahdizadeh, S. J. & Akhlagi, G. Optimized Tersoff empirical potential for germanene. *J. Mol. Graph. Model.* **72**, 1–5 (2017).

104. Tersoff, J. Modeling solid-state chemistry: interatomic potentials for multi-component systems. *Phys. Rev. B* **39**, 5566–5568 (1989).
105. Jiang, J.-W. & Wang, J.-S. Theoretical study of thermal conductivity in single-walled boron nitride nanotubes. *Phys. Rev. B* **84**, 85439 (2011).
106. Liu, B. et al. Thermal conductivity of silicene nanosheets and the effect of isotopic doping. *J. Phys. D: Appl. Phys.* **47**, 165301 (2014).
107. McGuigan, B. C., Pochet, P. & Johnson, H. T. Critical thickness for interface misfit dislocation formation in two-dimensional materials. *Phys. Rev. B* **93**, 214103 (2016).
108. Raju, M., van Duin, A. & Ihme, M. Phase transitions of ordered ice in graphene nanocapillaries and carbon nanotubes. *Sci. Rep.* **8**, 3851 (2018).
109. Huang, X., Yang, H., van Duin, A. C. T., Hsia, K. J. & Zhang, S. Chemomechanics control of tearing paths in graphene. *Phys. Rev. B* **85**, 195453 (2012).
110. Paupitz, R. et al. Graphene to fluorographene and fluorographene: a theoretical study. *Nanotechnology* **24**, 35706 (2012).
111. Neyts, E. C., van Duin, A. C. T. & Bogaerts, A. Formation of single layer graphene on nickel under far-from-equilibrium high flux conditions. *Nanoscale* **5**, 7250–7255 (2013).
112. Achtyl, J. L. et al. Aqueous proton transfer across single-layer graphene. *Nat. Commun.* **6**, 6539 (2015).
113. Raju, M., Govindaraju, P. B., van Duin, A. C. T. & Ihme, M. Atomistic and continuum scale modeling of functionalized graphyne membranes for water desalination. *Nanoscale* **10**, 3969–3980 (2018).
114. Berdiyrov, G. R., Neek-Amal, M., Peeters, F. M. & van Duin, A. C. T. Stabilized silicene within bilayer graphene: a proposal based on molecular dynamics and density-functional tight-binding calculations. *Phys. Rev. B* **89**, 24107 (2014).
115. Berdiyrov, G. R. & Peeters, F. M. Influence of vacancy defects on the thermal stability of silicene: a reactive molecular dynamics study. *RSC Adv.* **4**, 1133–1137 (2014).
116. Kushima, A., Qian, X., Zhao, P., Zhang, S. & Li, J. Riplocations in van der Waals layers. *Nano Lett.* **15**, 1302–1308 (2015).
117. Yilmaz, D. E., Lotfi, R., Ashraf, C., Hong, S. & van Duin, A. C. T. Defect design of two-dimensional MoS₂ structures by using a graphene layer and potato stamp concept. *J. Phys. Chem. C* **122**, 11911–11917 (2018).
118. Mortazavi, B. et al. Strong thermal transport along polycrystalline transition metal dichalcogenides revealed by multiscale modeling for MoS₂. *Appl. Mater. Today* **7**, 67–76 (2017).
119. Yan, R. et al. Thermal conductivity of monolayer molybdenum disulfide obtained from temperature-dependent Raman spectroscopy. *ACS Nano* **8**, 986–993 (2014).
120. Osti, N. C. et al. Effect of metal ion intercalation on the structure of MXene and water dynamics on its internal surfaces. *ACS Appl. Mater. Interfaces* **8**, 8859–8863 (2016).
121. Berdiyrov, G. R. & Mahmoud, K. A. Effect of surface termination on ion intercalation selectivity of bilayer Ti₃C₂T₂(T=F, O and OH) MXene. *Appl. Surf. Sci.* **416**, 725–730 (2017).
122. Osti, N. C. et al. Influence of metal ions intercalation on the vibrational dynamics of water confined between MXene layers. *Phys. Rev. Mater.* **1**, 65406 (2017).
123. Overbury, S. H. et al. Complexity of intercalation in MXenes: destabilization of urea by two-dimensional titanium carbide. *J. Am. Chem. Soc.* **140**, 10305–10314 (2018).
124. Sang, X. et al. In situ atomistic insight into the growth mechanisms of single layer 2D transition metal carbides. *Nat. Commun.* **9**, 2266 (2018).
125. Wang, N. & Komvopoulos, K. The effect of deposition energy of energetic atoms on the growth and structure of ultrathin amorphous carbon films studied by molecular dynamics simulations. *J. Phys. D: Appl. Phys.* **47**, 245303 (2014).
126. Ma, T., Hu, Y.-Z., Wang, H. & Li, X. Microstructural and stress properties of ultrathin diamondlike carbon films during growth: Molecular dynamics simulations. *Phys. Rev. B* **75**, 35425 (2007).
127. Wang, X., Tabarraei, A. & Spearot, D. E. Fracture mechanics of monolayer molybdenum disulfide. *Nanotechnology* **26**, 175703 (2015).
128. Reddy, C. D., Gen Yu, Z. & Zhang, Y.-W. Two-dimensional van der Waals C₆₀ molecular crystal. *Sci. Rep.* **5**, 12221 (2015).
129. Paul, S. & Momeni, K. Mechanochemistry of stable diamane and atomically thin diamond films synthesis from bi- and multilayer graphene: a computational study. *J. Phys. Chem. C* **123**, 15751–15760 (2019).
130. Edward, L.-J. J. & Sydney, C. On the forces between atoms and ions. *Proc. R. Soc. A Math. Phys. Eng. Sci.* **109**, 584–597 (1925).
131. Cheng, Y.-T. et al. Cu cluster deposition on ZnO(101̄0): morphology and growth mode predicted from molecular dynamics simulations. *Surf. Sci.* **621**, 109–116 (2014).
132. Cui, L., Shi, S., Li, Z., Wei, G. & Du, X. Manipulating thermal conductance of supported graphene via surface hydroxylation of substrates. *J. Phys. Chem. C* **122**, 27689–27695 (2018).
133. Burton, W. K., Cabrera, N., Frank, F. C. & Francis, M. N. The growth of crystals and the equilibrium structure of their surfaces. *Philos. Trans. R. Soc. Lond. Ser. A, Math. Phys. Sci.* **243**, 299–358 (1951).
134. Steinbach, I. Phase-field model for microstructure evolution at the mesoscopic scale. *Annu. Rev. Mater. Res.* **43**, 89–107 (2013).
135. Liu, F. & Metiu, H. Stability and kinetics of step motion on crystal surfaces. *Phys. Rev. E* **49**, 2601–2616 (1994).
136. Karma, A. & Plapp, M. Spiral surface growth without desorption. *Phys. Rev. Lett.* **81**, 4444–4447 (1998).
137. Pierre-Louis, O. Phase field models for step flow. *Phys. Rev. E* **68**, 21604 (2003).
138. Hu, Z., Lowengrub, J. S., Wise, S. M. & Voigt, A. Phase-field modeling of epitaxial growth: applications to step trains and island dynamics. *Phys. D: Nonlinear Phenom.* **241**, 77–94 (2012).
139. Meca, E., Lowengrub, J., Kim, H., Mattevi, C. & Shenoy, V. B. Epitaxial graphene growth and shape dynamics on copper: phase-field modeling and experiments. *Nano Lett.* **13**, 5692–5697 (2013).
140. Meca, E., Shenoy, V. B. & Lowengrub, J. Phase-field modeling of two-dimensional crystal growth with anisotropic diffusion. *Phys. Rev. E* **88**, 52409 (2013).
141. Wu, J. et al. Spiral growth of SnSe₂ crystals by chemical vapor deposition. *Adv. Mater. Interfaces* **3**, 1600383 (2016).
142. Li, J. et al. Impurity-induced formation of bilayered graphene on copper by chemical vapor deposition. *Nano Res* **9**, 2803–2810 (2016).
143. Zhang, K. et al. Manganese doping of monolayer MoS₂: the substrate is critical. *Nano Lett.* **15**, 6586–6591 (2015).
144. Hao, Y. et al. The role of surface oxygen in the growth of large single-crystal graphene on copper. *Science* **342**, 720–723 (2013).
145. Luo, B. et al. Etching-controlled growth of graphene by chemical vapor deposition. *Chem. Mater.* **29**, 1022–1027 (2017).
146. Artyukhov, V. I., Hu, Z., Zhang, Z. & Yakobson, B. I. Topochemistry of Bowtie- and star-shaped metal dichalcogenide nanoisland formation. *Nano Lett.* **16**, 3696–3702 (2016).
147. Yu, H. et al. Tilt grain boundary topology induced by substrate topography. *ACS Nano* **11**, 8612–8618 (2017).
148. Meca, E., Shenoy, V. B. & Lowengrub, J. H. H₂-dependent attachment kinetics and shape evolution in chemical vapor deposition graphene growth. *2D Mater.* **4**, 31010 (2017).
149. Berry, J., Zhou, S., Han, J., Srolowitz, D. J. & Haataja, M. P. Dynamic phase engineering of bendable transition metal dichalcogenide monolayers. *Nano Lett.* **17**, 2473–2481 (2017).
150. Emmerich, H. et al. Phase-field-crystal models for condensed matter dynamics on atomic length and diffusive time scales: an overview. *Adv. Phys.* **61**, 665–743 (2012).
151. Elder, K. L. M., Seymour, M., Lee, M., Hilke, M. & Provatas, N. Two-component structural phase-field crystal models for graphene symmetries. *Philos. Trans. R. Soc. A Math. Phys. Eng. Sci.* **376**, 20170211 (2018).
152. Taha, D., Mkhonta, S. K., Elder, K. R. & Huang, Z.-F. Grain boundary structures and collective dynamics of inversion domains in binary two-dimensional materials. *Phys. Rev. Lett.* **118**, 255501 (2017).
153. Battaile, C. C. The kinetic Monte Carlo method: foundation, implementation, and application. *Comput. Methods Appl. Mech. Eng.* **197**, 3386–3398 (2008).
154. Nie, Y. et al. A kinetic Monte Carlo simulation method of van der Waals epitaxy for atomistic nucleation-growth processes of transition metal dichalcogenides. *Sci. Rep.* **7**, 2977 (2017).
155. Trevethan, T., Latham, C. D., Heggie, M. I., Briddon, P. R. & Rayson, M. J. Vacancy diffusion and coalescence in graphene directed by defect strain fields. *Nanoscale* **6**, 2978–2986 (2014).
156. Whitesides, R. & Frenklach, M. Effect of reaction kinetics on graphene-edge morphology and composition. *Z. für Physikalische Chem.* **229**, 597–614 (2015).
157. Wang, B., Puzryev, Y. S. & Pantelides, S. T. Enhanced chemical reactions of oxygen at grain boundaries in polycrystalline graphene. *Polyhedron* **64**, 158–162 (2013).
158. Zhuang, J., Zhao, R., Dong, J., Yan, T. & Ding, F. Evolution of domains and grain boundaries in graphene: a kinetic Monte Carlo simulation. *Phys. Chem. Chem. Phys.* **18**, 2932–2939 (2016).
159. Taioli, S. Computational study of graphene growth on copper by first-principles and kinetic Monte Carlo calculations. *J. Mol. Model.* **20**, 2260 (2014).
160. Fan, L. et al. Topology evolution of graphene in chemical vapor deposition, a combined theoretical/experimental approach toward shape control of graphene domains. *Nanotechnology* **23**, 115605 (2012).
161. Gaillard, P., Schoenhalz, A. L., Moskovkin, P., Lucas, S. & Henrard, L. Growth of nitrogen-doped graphene on copper: multiscale simulations. *Surf. Sci.* **644**, 102–108 (2016).
162. Wu, P. et al. Lattice mismatch induced nonlinear growth of graphene. *J. Am. Chem. Soc.* **134**, 6045–6051 (2012).

163. Jiang, H. & Hou, Z. Large-scale epitaxial growth kinetics of graphene: a kinetic Monte Carlo study. *J. Chem. Phys.* **143**, 84109 (2015).
164. Huang, J. Y. et al. In situ observation of graphene sublimation and multi-layer edge reconstructions. *Proc. Natl Acad. Sci. USA* **106**, 10103–10108 (2009).
165. Ming, F. & Zangwill, A. Model and simulations of the epitaxial growth of graphene on non-planar 6H–SiC surfaces. *J. Phys. D: Appl. Phys.* **45**, 154007 (2012).
166. Qiu, Z., Li, P., Li, Z. & Yang, J. Atomistic simulations of graphene growth: from kinetics to mechanism. *Acc. Chem. Res.* **51**, 728–735 (2018).
167. Nie, Y. et al. First principles kinetic Monte Carlo study on the growth patterns of WSe₂ monolayer. *2D Mater.* **3**, 25029 (2016).
168. Chen, S. et al. Origin of ultrafast growth of monolayer WSe₂ via chemical vapor deposition. *npj Comput. Mater.* **5**, 28 (2019).
169. Yue, R. et al. Nucleation and growth of WSe₂: enabling large grain transition metal dichalcogenides. *2D Mater.* **4**, 45019 (2017).
170. Safron, N. S. & Arnold, M. S. Experimentally determined model of atmospheric pressure CVD of graphene on Cu. *J. Mater. Chem. C* **2**, 744–755 (2014).
171. Eversteyn, F. C., Severin, P. J. W., Brekel, C. H. Jvd & Peek, H. L. A stagnant layer model for the epitaxial growth of silicon from silane in a horizontal reactor. *J. Electrochem. Soc.* **117**, 925–931 (1970).
172. Chen, J., Wong, D. S. H., Jang, S. S. & Yang, S. L. Product and process development using artificial neural-network model and information analysis. *AIChE J.* **44**, 876–887 (1998).
173. Vilà, R. A. et al. Bottom-up synthesis of vertically oriented two-dimensional materials. *2D Mater.* **3**, 41003 (2016).
174. Lee, P. W., Omstead, T. R., McKenna, D. R. & Jensen, K. F. In situ mass spectroscopy studies of the decomposition of organometallic arsenic compounds in the presence of Ga(CH₃)₃ and Ga(C₂H₅)₃. *J. Cryst. Growth* **93**, 134–142 (1988).
175. Theodoropoulos, C. et al. Kinetic and transport modeling of the metallorganic chemical vapor deposition of InP from trimethylindium and phosphine and comparison with experiments. *J. Electrochem. Soc.* **142**, 2086–2094 (1995).
176. Poling, B. E., Prausnitz, J. M. & O'Connell, J. P. *The Properties of Gases and Liquids*, Vol. 5 (Mcgraw-Hill, New York, 2001).
177. Zhang, F. et al. Controlled synthesis of 2D transition metal dichalcogenides: from vertical to planar MoS₂. *2D Mater.* **4**, 25029 (2017).
178. Grazulis, S. et al. Crystallography open database - an open-access collection of crystal structures. *J. Appl. Crystallogr.* **42**, 726–729 (2009).
179. Belsky, A., Hellenbrandt, M., Karen, V. L. & Luksch, P. New developments in the Inorganic Crystal Structure Database (ICSD): accessibility in support of materials research and design. *Acta Crystallogr. Sect. B* **58**, 364–369 (2002).
180. Allen, F. H. et al. The Cambridge Crystallographic Data Centre: computer-based search, retrieval, analysis and display of information. *Acta Crystallogr. Sect. B* **35**, 2331–2339 (1979).
181. Choudhary, K., Kalish, I., Beams, R. & Tavazza, F. High-throughput identification and characterization of two-dimensional materials using density functional theory. *Sci. Rep.* **7**, 5179 (2017).
182. Haastrup, S. et al. The Computational 2D Materials. Database.: high-throughput modeling Discov. *atomically thin Cryst.* *2D Mater.* **5**, 42002 (2018).
183. Cheon, G. et al. Data mining for new two- and one-dimensional weakly bonded solids and lattice-commensurate heterostructures. *Nano Lett.* **17**, 1915–1923 (2017).
184. Ashton, M., Paul, J., Sinnott, S. B. & Hennig, R. G. Topology-scaling identification of layered solids and stable exfoliated 2D materials. *Phys. Rev. Lett.* **118**, 106101 (2017).
185. Patra, T. K. et al. Defect dynamics in 2-D MoS₂ probed by using machine learning, atomistic simulations, and high-resolution microscopy. *ACS Nano* **12**, 8006–8016 (2018).
186. Tawfik, S. A. et al. Efficient prediction of structural and electronic properties of hybrid 2D materials using complementary DFT and machine learning approaches. *Adv. Theory Simul.* **2**, 1800128 (2019).
187. Choudhary, K., DeCost, B. & Tavazza, F. Machine learning with force-field-inspired descriptors for materials: fast screening and mapping energy landscape. *Phys. Rev. Mater.* **2**, 83801 (2018).
188. Eivari, H. A. et al. Two-dimensional hexagonal sheet of TiO₂. *Chem. Mater.* **29**, 8594–8603 (2017).
189. Miyazato, I., Tanaka, Y. & Takahashi, K. Accelerating the discovery of hidden two-dimensional magnets using machine learning and first principle calculations. *J. Phys. Condens. Matter* **30**, 06LT01 (2018).
190. Cherukara, M. J. et al. Ab initio-based bond order potential to investigate low thermal conductivity of stanene nanostructures. *J. Phys. Chem. Lett.* **7**, 3752–3759 (2016).
191. Revard, B. C., Tipton, W. W., Yesypenko, A. & Hennig, R. G. Grand-canonical evolutionary algorithm for the prediction of two-dimensional materials. *Phys. Rev. B* **93**, 54117 (2016).
192. Singh, A. K. et al. Genetic algorithm prediction of two-dimensional group-IV dioxides for dielectrics. *Phys. Rev. B* **95**, 155426 (2017).
193. Chmiela, S. et al. Machine learning of accurate energy-conserving molecular force fields. *Sci. Adv.* **3**, e1603015 (2017).
194. Botu, V., Batra, R., Chapman, J. & Ramprasad, R. Machine learning force fields: construction, validation, and outlook. *J. Phys. Chem. C* **121**, 511–522 (2017).
195. Song, Z., Artyukhov, V. I., Yakobson, B. I. & Xu, Z. Pseudo Hall–Petch strength reduction in polycrystalline graphene. *Nano Lett.* **13**, 1829–1833 (2013).
196. Okada, M. et al. Direct chemical vapor deposition growth of WS₂ atomic layers on hexagonal boron nitride. *ACS Nano* **8**, 8273–8277 (2014).
197. Kobayashi, Y. et al. Growth and optical properties of high-quality monolayer WS₂ on graphite. *ACS Nano* **9**, 4056–4063 (2015).
198. Huang, J. et al. Large-area synthesis of monolayer WSe₂ on a SiO₂/Si substrate and its device applications. *Nanoscale* **7**, 4193–4198 (2015).
199. Chen, L. et al. Step-edge-guided nucleation and growth of aligned WSe₂ on sapphire via a layer-over-layer growth mode. *ACS Nano* **9**, 8368–8375 (2015).
200. Eichfeld, S. M. et al. Highly scalable, atomically thin WSe₂ grown via metal–organic chemical vapor deposition. *ACS Nano* **9**, 2080–2087 (2015).
201. Yanase, T. et al. Chemical vapor deposition of NbS₂ from a chloride source with H₂ Flow: orientation control of ultrathin crystals directly grown on SiO₂/Si substrate and charge density wave transition. *Cryst. Growth Des.* **16**, 4467–4472 (2016).
202. Friday, M., Angeles, L., Reyes-lillo, S. & Rabe, K. *Bulletin of the American Physical Society APS March Meeting 2018*. **2018** (2018).
203. Hotta, T. et al. Molecular beam epitaxy growth of monolayer niobium diselenide flakes. *Appl. Phys. Lett.* **109**, 133101 (2016).
204. Efetov, D. K. et al. Specular interband Andreev reflections at van der Waals interfaces between graphene and NbSe₂. *Nat. Phys.* **12**, 328–332 (2016).
205. Zhou, L. et al. Large-area synthesis of high-quality uniform few-layer MoTe₂. *J. Am. Chem. Soc.* **137**, 11892–11895 (2015).
206. Farahani, H., Rajabpour, A. & Reyhani, A. Interfacial thermal resistance between few-layer MoS₂ and silica substrates: a molecular dynamics study. *Comput. Mater. Sci. J.* **142**, 1–6 (2018).
207. Hong, Y., Ju, M. G., Zhang, J. & Zeng, X. C. Phonon thermal transport in a graphene/MoSe₂ van der Waals heterobilayer. *Phys. Chem. Chem. Phys.* **20**, 2637–2645 (2018).
208. Filippova, V. P., Kunavin, S. A. & Pugachev, M. S. Calculation of the parameters of the Lennard-Jones potential for pairs of identical atoms based on the properties of solid substances. *Inorg. Mater. Appl. Res.* **6**, 1–4 (2015).
209. Al-Matar, A. K. & Rockstraw, D. A. A generating equation for mixing rules and two new mixing rules for interatomic potential energy parameters. *J. Comp. Chem.* **25**, 660–668 (2004).
210. Hiura, H., Miyazaki, T. & Kanayama, T. Formation of metal-encapsulating Si cage clusters. *Phys. Rev. Lett.* **86**, 1733–1736 (2001).
211. Mundin, K. C. & Ellis, D. E. Stochastic classical molecular dynamics coupled to functional density theory: applications to large molecular systems. *Braz. J. Phys.* **29**, 199–214 (1999).
212. Morris, G. M. et al. *van Der Waals Potential Energy* (2003). Available at: <http://www.img.bio.uni-goettingen.de/mswww/internal/manuals/autodock/AD3.a0UserGuide.html> (Accessed 23 March 2019).
213. Lewis, L. J. & Mousseau, N. Tight-binding molecular-dynamics studies of defects and disorder in covalently bonded materials. *Comput. Mater. Sci.* **12**, 210–241 (1998).
214. Turner, G. W., Chushak, Y. G. & Bartell, L. S. Molecular dynamics investigation of transient nucleation in the freezing of clusters of SeF₆. *J. Phys. Chem. A* **108**, 1666–1670 (2004).
215. Monajjemi, M., Ketabi, S., Hashemian Zadeh, M. & Amiri, A. Simulation of DNA bases in water: comparison of the Monte Carlo algorithm with molecular mechanics force fields. *Biochem* **71**, S1–S8 (2006).
216. Landron, C. et al. Liquid alumina: detailed atomic coordination determined from neutron diffraction data using empirical potential structure refinement. *Phys. Rev. Lett.* **86**, 4839–4842 (2001).
217. Bartell, L. S. & Xu, S. Molecular dynamics examination of an anomalous phase of TeFe molecules. *J. Phys. Chem.* **95**, 8939–8941 (1991).

ACKNOWLEDGEMENTS

K.M. and L.Q.C. are partially supported by the Hamer Professorship at Penn State, Louisiana Tech University, the National Science Foundation 2D Crystal Consortium –

Material Innovation Platform (2DCC-MIP) under NSF cooperative agreement DMR-1539916, and the NSF-CAREER under NSF cooperative agreement CBET-1943857. Y.Z. J. is supported by the I/UCRC Center for Atomically Thin Multifunctional Coatings (ATOMIC) seed project SP001-17 and the 2DCC-MIP. This project is also partly supported by DoE-ARPA-E OPEN, NASA-EPSCoR, Louisiana EPSCoR-OIA-1541079 (NSF (2018)-CIMMSeed-18 and NSF(2018)-CIMMSeed-19), and LEQSF(2015-18)-LaSPACE. J. W.J. is supported by the Recruitment Program of Global Youth Experts of China, the National Natural Science Foundation of China (NSFC) under Grant Number 11822206, and the Innovation Program of Shanghai Municipal Education Commission under Grant Number 2017-01-07-00-09-E00019. H.S.P. acknowledges the support of the Mechanical Engineering Department at Boston University. A.C.T.v.D., D.Y., and Y.S. acknowledge funding from the Fluid Interface Reactions, Structures and Transport (FIRST) Center, an Energy Frontier Research Center funded by the U.S. Department of Energy (DOE), Office of Science, Basic Energy Science for MXene force-field development and application work.

AUTHOR CONTRIBUTIONS

All authors contributed to collecting the references and outlining the review paper. K.M. drafted the review. All authors participated in revising the manuscript.

COMPETING INTERESTS

The authors declare no competing interests.

ADDITIONAL INFORMATION

Correspondence and requests for materials should be addressed to K.M.

Reprints and permission information is available at <http://www.nature.com/reprints>

Publisher's note Springer Nature remains neutral with regard to jurisdictional claims in published maps and institutional affiliations.



Open Access This article is licensed under a Creative Commons Attribution 4.0 International License, which permits use, sharing, adaptation, distribution and reproduction in any medium or format, as long as you give appropriate credit to the original author(s) and the source, provide a link to the Creative Commons license, and indicate if changes were made. The images or other third party material in this article are included in the article's Creative Commons license, unless indicated otherwise in a credit line to the material. If material is not included in the article's Creative Commons license and your intended use is not permitted by statutory regulation or exceeds the permitted use, you will need to obtain permission directly from the copyright holder. To view a copy of this license, visit <http://creativecommons.org/licenses/by/4.0/>.

© The Author(s) 2020